UNIVERSITY OF CALIFORNIA,

IRVINE

Evaluating Mitochondria Transfer, Energy Metabolism, ROS Accumulation, and Development of Fluctuation Correlation using the side-SPIM

DISSERTATION

submitted in satisfaction of the requirements

for the degree of

DOCTOR OF PHILOSOPHY

in Biomedical Engineering

by

Yu-Kai Huang

Dissertation Committee:
Associate Professor Michelle Digman, Chair
Associate Professor Jered Haun
Associate Professor Manabu Shiraiwa

2023

DEDICATION

To my family

你們的支持我無以回報

Table of Contents

List of Figures

ACKNOWLEDGEMENTS

I express my most sincere appreciation to all the people who participated in my life and shaped of what I am today.

To my family, you have been the fundamental of my passion to science in every kind of ways. To Dr. Chiaping Huang, thank you for giving me this dream life starting from your Ph.D. career in UK. I have always worked to be the son who can make you proud of, but your philosophy teaches me to embrace what we deserve and hence let me live without much pressure. To Chiuwen Chiang, thank you for giving birth to me and the chance to experience this world since day one of my life. No matter how far away I am from God, you will always be the first to remind me to have faith in his name. To Chunyen Huang, thank you my dearest little brother for being a more independent son than I am and took care of our parents during my study abroad. To grandma In, grandma Shen, aunt Theresa, uncle Jason, and the whole family, thank you for providing a complete home back in Taiwan. To uncle Jordan and his family, thank you for taking care of my living in the US. You have treated me as another son, and it was a privilege being invited to your house every holiday to gain much weight.

To NTNUME fellows, Ballson, Deep, Albert, Baron, Tony, Ted, and Christine. You have been able to fuel me up whenever I visit Taiwan. Those surfing, road trips, and drinking crazy could only define the slightest of our friendship. Thank you for holding my back and persuade me to believe in my decisions. To Signal Processing lab, Dr. Shuende Wu, Songru, and Xiucheng, thank you for putting together our final project which became the trigger leading me towards biomedical imaging. To Leonard and James, thank you for standing by my side ever since high school. Although we have strived totally different pathways but never have we separated in life.

To the UCI badminton club, thank you all for the wonderful time outside of research, especially when it comes to late-night hangouts (Caines?). To Dakota, Eric, Tom, and Jerry, thank you for the long last coach gang and what we have accomplished in league matches and open games.

To P5, Evan, Shawn, Sungsik, Pisrut, and Becky, grad life would never be as fun if we did not meet in our first year. The usual end of quarter Eureka meetup, the boba treating after publishing papers, and now we have finally made it to the end. P5 has finally evolved from pathetic to fantastic lives.

Thank you to the American Chemical Society and Multidisciplinary Digital Publishing Institute for permission to include portions of my dissertation.

I would like to take the opportunity to thank the many mentors, colleagues, and collaborators who helped me throughout this thesis.

First and most importantly, thank you to my advisor, Dr. Michelle Digman, who gave inspiration to all the ideas happened in this dissertation. Your guidance and encouragement led me across all obstacles I have faced. I could never forget the first time walking in your office asking for a rotation opportunity with no clue of what FLIM is while you patiently explained all the potential projects I could work on. Thank you, Dr. Enrico Gratton, for watching over my needs of every experiments performed in each and every microscope you own. Your enthusiasm towards science and education is a never-ending fire that continues to inspire young fellows like me.

To my collaborator, Dr. Manabu Shiraiwa, Dr. Ting Fang, and Dr. Jinlai Wei, thank you for giving me the opportunity to engage in such a large-scale project and willing to join me in every late night experiments.

To the LFD, thank you Dr. Hongtao Chen for being my first microscopy mentor enabling me to open doors toward the various instrumentations used in research. A huge appreciation goes to Dr. Per Niklas Hedde who trained me to become the master of side-SPIM and influenced me the most in becoming a solid engineer capable of performing magnificent science. Thank you, Dr. Alexander Vallmitjana Lees, Dr. Francesco Palomba, Dr. Belén Torrado Rodríguez, and Dr. Lorenzo Scipioni who were always on the name list whenever I had problems on lab stuff or future career. A special thanks goes to Dr. Austin Lefebvre and Giulia who were not afraid to babysit a non-bio background student like me wondering what to do in cell culture rooms and always answering my dumb questions. Thank you to Balam, Song, Karen, and Ashley who are the young generation of Digman lab reminding me to stay passionate in experiments no matter how many times the FLIMbox or two-photon does not work. Thank you to my one and only undergraduate student, Mary Zhuang, who always took good care of the tasks I distributed and followed my lead to numerous data analysis.

Lastly, I would like to thank Jessica Sui, who although is not in research field but deserves more than me to be in every author list of my publications. Thank you for your unconditional care and support which carried me throughout the hardest days of my PhD. You are and always the light in my heart.

VITA

Yu-Kai Huang

EDUCATION

Ph.D. in Biomedical Engineering **2023**
University of California, Irvine Irvine, California

M.S. in Biomedical Engineering **2021**
University of California, Irvine Irvine, California

B.E. in Mechatronics Engineering **2016**
National Taiwan Normal University Taipei, Taiwan

RESEARCH EXPERIENCE

Laboratory for Fluorescence Dynamics **2019-2023**
University of California, Irvine Irvine, California

Signal Processing Lab **2014-2016**
National Taiwan Normal University Taipei, Taiwan

TEACHING EXPERIENCE

Teaching Assistant, BME 60c **2023**
University of California, Irvine Irvine, California

Lecturer, LFD workshop **2021-2022**
University of California, Irvine Irvine, California

Team Leader, USIBR **2022**
University of California, Irvine Irvine, California

Teaching Assistant, Applied Electronics Lab **2015-2016**
National Taiwan Normal University Taipei, Taiwan

Lecturer **2012-2015**
Taidai Institute Taipei, Taiwan

PUBLICATIONS

Yu-Kai Huang, Michelle A. Digman, "Determining Metabolism Shift of Mitochondria Transfer using Phasor Approach FLIM", Communications biology, under review (**2023**)

Yu-Kai Huang, Per Niklas Hedde, "Breaking the concentration limit in fluorescence fluctuation spectroscopy with camera-based detection", Macromolecules. International Journal of Molecular Sciences 23 (17), 9840 (**2022**)

Ting Fang, **Yu-Kai Huang**, Jinlai Wei, Jessica Monterrosa Mena, Pascale Lakey, Michael Kleinman, Michelle Digman, Manabu Shiraiwa, "Superoxide Release by Macrophages Dominates over Aqueous Chemistry of Secondary Organic Aerosols in Epithelial Lining Fluid", Environmental Science & Technology Article ASAP. DOI: 10.1021/acs.est.2c03987. (**2022**)

Barbara Barylko, Per Niklas Hedde, Clinton A. Taylor, Der D. Binns, **Yu-Kai Huang**, Gemma Molinaro, Kimberly M. Huber, David M. Jameson, and Joseph P. Albanesi, "Palmitoylation-regulated interactions of the pseudokinase calmodulin kinase-like vesicle-associated with membranes and Arc/Arg3. 1", Front. Synaptic Neurosci. Volume 14. (**2022**)

Yu-Kai Huang, Chia-Ping Huang, "An Optimization Image Segmentation Clustering Algorithm for Badminton Sport Moving Tracking Applications from Video Sequences", IJCSIS volume 15 No.7. (**2017**)

PRESENTATIONS

Yu-Kai Huang, Mary Zhuang, Michelle A. Digman, "Metabolic Profiling of Transferred Mitochondria Using FLIM Intensity Based Image Segmentation (FIBIS)", Biophysical Society Annual Meeting, Optical Microscopy and Super resolution Imaging I, San Diego (**2023**)

Yu-Kai Huang, Michelle A. Digman, "Determining Metabolism Shift of Mitochondria Transfer using the Phasor Approach to FLIM", Biomedical Engineering Society (BMES) Annual Meeting, biomedical imaging and instrumentation, San Antonio (**2022**)

Yu-Kai Huang, Michelle A. Digman, "Determining Metabolism Shift of Mitochondria Transfer using the Phasor Approach to FLIM", 22nd Annual UC Systemwide Bioengineering Symposium, Santa Barbara (**2022**)

Yu-Kai Huang, Ting Fang, Jinlai Wei, Jessica E.M. Mena, Pascale S.J. Lakey, Michael T. Kleinman, Manabu Shiraiwa, Michelle A. Digman, "Phasor Approach FLIM as an Indicator for NADPH Oxidase During Exposure to Secondary Organic Aerosols", 11th Annual Southern California Systems Biology Symposium, Los Angeles (**2022**)

Yu-Kai Huang, Michelle A. Digman, "Metabolism shift of Epithelial Mitochondria Transplantation in Breast Cancer cells Based on Phasor FLIM", Cell Bio virtual (**2020**)

Yu-Kai Huang, C. P. Huang, "A Depth-First Search Algorithm Based Otoscope Application for Real-time Otitis Media Image Interpretation", 18th International Conference on Parallel and Distributed Computing, Applications and Technologies (PDCAT) , Taipei (**2017**)

HONORS AND AWARDS

Student Research Achievement Award **2023**
67TH Biophysical Society Annual Meeting

Graduate Student Travel Award **2022**
22nd Annual UC Systemwide Bioengineering Symposium

Undergraduate Research Project Best Poster Award **2016**
National Taiwan Normal University

MOST Funded Undergraduate Research Project **2015**
Ministry Of Science and Technology

ABSTRACT OF THE DISSERTATION

Evaluation of Epithelial Mitochondria Transfer and Stimulated Reactive Oxygen Species via Fluorescence Lifetime Imaging Microscopy

By

Yukai Huang

Doctor of Philosophy in Biomedical Engineering

University of California, Irvine

Associate Professor Michelle Digman, Chair

The transfer of mitochondria, whether through natural or artificial pathways, has been experimentally validated across various cell lines, demonstrating potential benefits for host cells experiencing mitochondrial dysfunction. However, conflicting reports suggest that our understanding of the outcomes of mitochondria transfer in host cells remains incomplete. This dissertation aims to delve into the concept of mitochondria transfer and examine its effects on metabolism, viability, and oxidative stress in breast cancer host cells. The novelty of this dissertation lies in the utilization of fluorescence lifetime imaging to analyze the metabolic profiles of individual mitochondria. Through the combination of fluorescence labeling and NADH lifetime imaging, we have discovered that newly formed mitochondria in breast cancer host cells exhibit an increase in the bound fraction of NADH, indicating a reliance on Oxidative Phosphorylation (OXPHOS). While the enhancement of OXPHOS leads to heightened

respiration and proliferation, the accumulation of reactive oxygen species (ROS) levels surpasses the tolerance threshold of breast cancer cells towards oxidative stress, resulting in elevated drug sensitivity when exposed to anticancer drugs. The significance of this dissertation resides in its multifaceted approach, shedding light on the impact of mitochondria transfer and establishing new methodologies for future research endeavors.

CHAPTER 1. INTRODUCTION

1.1 Mitochondria transfer

Mitochondria transfer was first discovered in 2004 where Rustom et al[1] observed a natural pathway, referred as tunneling nanotubes (TNTs), in between rat pheochromocytoma PC12 cells that could transport organelles. The finding immediately raised various questions in the biological science field that need to be answered such as the mechanism and outcome of mitochondria being exchanged. Recent studies have demonstrated that in cases where cells containing dysfunctional mitochondria are unable to maintain homeostasis, they may release signals that facilitate intercellular communication and ultimately lead to the transfer of healthy mitochondria from neighboring cells[2,3] (Fig. 1.1). As the use of fluorescent microscopy imaging and cell assay development become more mature, scientists have discovered that mitochondria not only transfer naturally through TNTs, extracellular vesicles, or cell fusion, but could also be achieved through artificial approaches by isolating them from cell or tissue[4,5]. Isolation process significantly increases the production of pure mitochondria and efficiency of recipient cell uptake which makes the evaluation of transferred mitochondria more systematic instead of searching for cell-cell interaction events. Other works have improved the consumption rate of isolated mitochondria to better target and investigate recipient cells such as centrifugation (Mitoception), Microinjection, and Magnetomitotransfer[6–9]. Engineering

approaches help profit the happening of mitochondria transfer events while the evaluation of the effect still relies on metabolic assays which will be discussed in the next part.

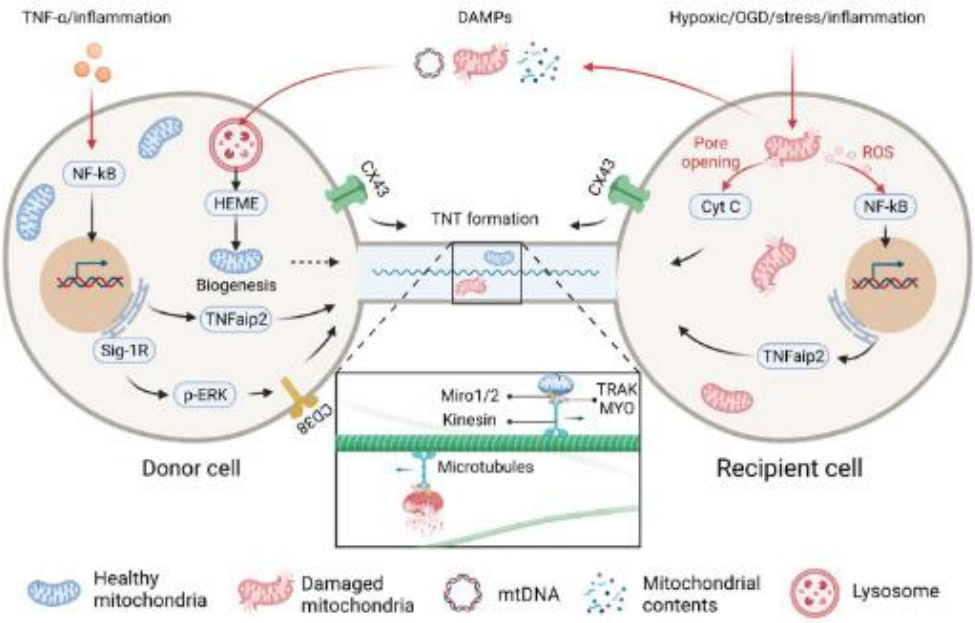

Figure 1. 1 Schematic graph of mitochondria transfer. Cells which contain damaged mitochondria usually gives out stress signals (DAMPs) to initiate material absorption, trafficking, processing, and integration. Once receiving stress signal, donor cells activate biogenesis for additional mitochondria ready to be exported through TNTs. ROS levels play a crucial role in forming these tunneling structures where within are microtubules which binds with Miro1 and 2 proteins to transport healthy mitochondria to recipient cells. Figure from Liu (2022). Reprint with permission from Springer Nature.

1.2 Cellular Metabolic Reaction to Mitochondria Transfer

After discovering the existence of mitochondria transfer, Spees et al[10] were the first to apply this technique to help save mitochondria depleted PC12 ρ cells from respiratory dysfunction. This proved that recipient cells are capable of consuming exogenous mitochondria and continue using these healthy mitochondria to signal intracellular function. Given that Spee et al's research has shed light on the potential therapeutic applications of mitochondrial transfer

for host cells with dysfunctional mitochondria, it is reasonable to investigate this phenomenon from a metabolic standpoint. However, the outcome remains controversial when studying different recipient cell lines since various assay measurements have been applied in a non-systematic manner[11–13]. One of the main reasons is that these assays do not specifically characterize recipient cell fate but measure the whole well in plate readers which could be insignificant or not sensitive enough for subtle changes in between cell interactions.

There are several cell-based assays that can be used to measure metabolism such as the Seahorse XF Assay which measures the extracellular acidification rate (ECAR) and the oxygen consumption rate (OCR) of cells[14]. ECAR is a measure of glycolysis, while OCR is a measure of oxidative phosphorylation. This assay is commonly used to measure the metabolic response of cells to different treatments. Another well-known assay called mitochondrial function assay[15] measures the function of mitochondria in cells. Mitochondria are labeled with a fluorescent dye, and the fluorescence intensity is measured. This assay is commonly used to measure the effect of drugs or other treatments on mitochondrial function. Lastly, the ratio of NAD+/NADH[16] indicates the cellular metabolism where these coenzymes involve in many metabolic pathways such as glycolysis, the TCA cycle, and oxidative phosphorylation. All these assays will be mentioned in this thesis which provide insight and supporting information of metabolic changes of host cancer cells after mitochondria transfer.

1.3 Reactive Oxygen Species

Reactive oxygen species (ROS) are highly reactive molecules that contain oxygen and are formed as by-products of normal cellular metabolism[17]. This includes molecules such as superoxide, hydrogen peroxide, and hydroxyl radicals, which are highly reactive and can cause damage to cells and tissues. As the core of cellular metabolism, mitochondria are the primary site of ROS production within cells, as a byproduct of the electron transport chain during ATP synthesis. Other intracellular factors, such as NADPH oxidases (NOX) and Xanthine oxidase, also produce decent amount of ROS that may influence the occurrence of DNA damage, mitochondrial dysfunction, and lipid peroxidation[18–20]. Overall, the damage caused by ROS when overwhelmed can have wide-ranging effects on cellular function and contribute to the development of many diseases, including cancer, cardiovascular disease, and neurodegenerative disorders[21]. To prevent the surpassing of intracellular ROS levels, monitoring of ROS production is critical to avoid the cascade reactions of free radicals which will be discussed in this thesis.

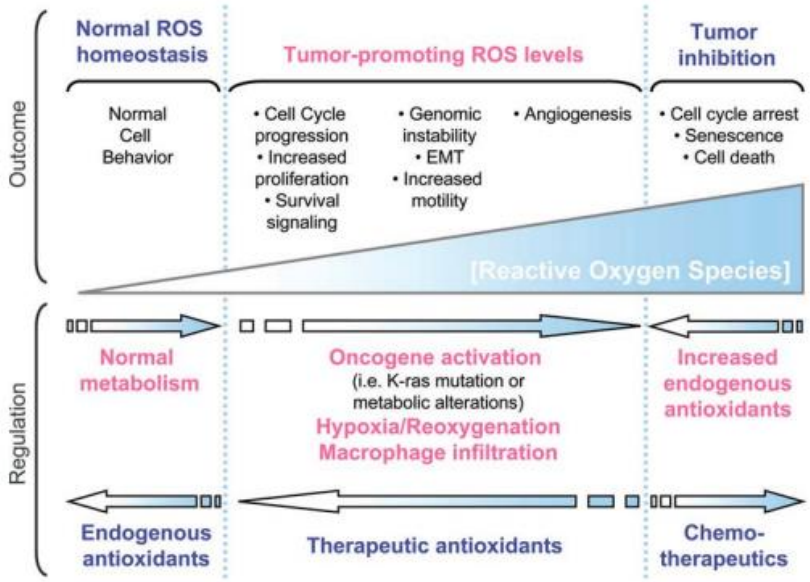

Figure 1. 2 Reactive oxygen species level effects to cells. ROS is naturally generated in cellular process and are depleted when exceeding normal metabolism threshold by antioxidants. Increase in intracellular ROS levels could activate tumorigenic events such as oncogene activation (i.e. mutation of K-ras). Tumor promoting ROS levels can lead to cell cycle progression, increased proliferation and survival signalling, EMT, increased motility, genomic instability and increased angiogenesis and may be negatively-regulated by therapeutic antioxidants. Yet, overwhelming ROS levels, such as stimulated ROS from anticancer drugs, can induce ell cycle arrest, senescence or cell death of tumour cells, but may be repulsed by the tumour cells through an increase in the expression of endogenous antioxidants. Figure from Liou (2010). Reprinted with permission from Taylor &Francis Online.

1.4 Spheroid imaging in light sheet microscopy

Light sheet microscopy is a powerful imaging technique that has emerged as a useful tool to study the dynamics of 3D cell cultures[22], including spheroids. Unlike traditional microscopy techniques, which rely on imaging a thin slice of the sample at a time, light sheet microscopy illuminates the sample with a thin plane of light, allowing for fast, high-resolution, and non-invasive imaging of the entire sample. One of the advantages of light sheet microscopy for imaging spheroids is its ability to capture high-resolution images of large samples in a short amount of time, with minimal photobleaching and phototoxicity. It also allows for live-cell

imaging, which can reveal the dynamics of cellular processes in real-time. However, light sheet microscopy requires specialized equipment and expertise, which can limit its accessibility to some researchers. The side-SPIM system from the Laboratory for Fluorescence Dynamics provides a user-friendly and customized platform for light sheet imaging.

1.5 Overview of the dissertation

In this dissertation, characteristics of cancer cell metabolism, mitochondrial dynamics, and ROS levels will be quantified by various imaging techniques. Chapter 2 and 3 covers the detailed measurements and verification of mitochondria transfer. In specifically, Chapter 2 investigates detailed information regarding the internalization and structural characteristics of mitochondria through confocal fluorescence microscopy. Furthermore, we discuss its subsequent impact on cancer cells as the roll of host cells through anticancer treatments.

In Chapter 3, we applied the Phasor approach to FLIM[23–27] to non-invasively indicate cellular metabolism after mitochondria transfer. To accentuate only single mitochondria information, we developed a FLIM intensity-based image segmentation (FIBIS) method to highlight NADH autofluorescence signal and improve the resolution of phasor approach FLIM from cellular to single mitochondria level.

In Chapter 4, we gained access into monitoring intracellular ROS levels and quantify acuteness of lipid peroxidation[28]. The intracellular ROS levels were stimulated by activation of NADPH

oxidase in macrophages, a defending mechanism in response to xenobiotic particles. Other than that, we first introduced the lifetime difference of Laurdan to indicate disorder of the cellular membrane resulting from the aggressive free radicals damaging unsaturated fatty acids.

To mimic true interactions of tumor in micro-environment, we discuss the use of light sheet microscopy in Chapter 5 where the side-SPIM system serves a suitable technique for cancer cell spheroid imaging. We tailored the imaging parameters to our specific requirements, including adjustments to filter wheels, exposure settings, and channel acquisition parameters. In more detail, we optimized the utilization of camera detector to study molecular dynamics in live cell compartments[29]. This demonstrates the capability of side-SPIM to track objects from molecular to organelle in live cells.

Finally, Chapter 6 summarizes the thesis work and provides future directions to potential applications.

CHAPTER 2. MITOCHONDRIA TRANSFER IN VIVO

2.1 Abstract

The transfer of mitochondria between cells has been a topic of interest in recent years due to its potential implications in various biological processes, including cancer progression and therapy. In this study, we aimed to validate the transfer of epithelial mitochondria to breast cancer cells and investigate the effects of this transfer on drug sensitivity. We utilized fluorescence labeling techniques to track the transfer of mitochondria and evaluate their localization within the recipient cells. Our results demonstrate successful transfer of epithelial mitochondria to breast cancer cells and an increase in drug sensitivity following the transfer. These findings suggest a potential therapeutic strategy for breast cancer treatment and highlight the importance of mitochondrial transfer in cancer biology.

2.2 Introduction

Mitochondria transfer or transplant refers to the transfer of mitochondria from one cell to another, typically in the context of medical treatments[30]. Mitochondria are organelles found within cells that play a critical role in energy production, and their dysfunction has been linked to a range of diseases, including neurological disorders and metabolic conditions[31,32]. In recent years, there has been increasing interest in using mitochondria transfer as a potential treatment approach. This involves transferring healthy mitochondria into cells with dysfunctional

mitochondria or even transplanting mitochondria from one individual to another. The happening of mitochondria transfer can occur naturally[33–35], such as during fertilization or immune cell-mediated transfer, or artificially [7–9,12,36], through the use of mitochondrial transplantation. While mitochondrial transfer has shown promise in treating certain diseases, such as mitochondrial diseases, there are also some contradicting aspects of its outcomes.

On the one hand, mitochondrial transfer can result in improved cellular function and increased energy production. Mitochondrial dysfunction can lead to a range of diseases, including neurodegenerative disorders, metabolic disorders, and cardiovascular diseases. In some cases, mitochondrial transfer has been shown to improve cellular function in cells with dysfunctional mitochondria, leading to increased ATP production and improved cellular function[37–39]. On the other hand, there is evidence that epithelial mitochondria can suppress tumor growth[40–42]. Epithelial cells are a type of cell that lines the surfaces of the body, including the lining of organs and glands[43]. These cells play a key role in the development and maintenance of tissues, and they have been implicated in the development of several types of cancer such as lung and breast cancer cells. The goal for this section is to elaborate outcomes of transferred mitochondria after entering breast cancer host cells through morphology dynamics and cell viability assays. While still a relatively new field, research into mitochondria transfer holds promise for developing new therapies for a range of conditions.

2.3 Material and Methods

2.3.1 Cell culture and labeling

MCF10A cells were cultured in Dulbecco's Modified Eagle's Medium (DMEM/F12) with high glucose, sodium pyruvate and L-glutamine (11320033 Thermo Fisher Scientific, Waltham, MA, USA) supplemented with 5% horse serum (26050088 Thermo Fisher Scientific, Waltham, MA, USA), 20 ng/mL epidermal growth factor, 0.5 mg/mL Hydrocortisone (H0888 Sigma-Aldrich),100 ng/mL cholera toxin (9012-63-9 Sigma-Aldrich), 10 μg/mL insulin (I3536 Sigma-Aldrich), and 1% Penicillin-Streptomycin 100X Solution (25-512 Genesee Scientific, San Diego, CA, USA). MCF7 and MDA-MB-231 cells were cultured in DMEM with high glucose, L-glutamate, and sodium pyruvate supplemented with 10% heat-inactivated Fetal Bovine Serum and 1% Penicillin-Streptomycin 100X solution. All cell lines were incubated at 37 °C, 5% CO2. For validation of mitochondria uptake, MCF10As were transfected with COX8GFP and MDA-MB-231 host cells were stably expressing mCherry. For mitochondrial dynamics experiments, MCF10As were transfected with Mito7-mRuby while MCF7 and MDA-MB-231s were transfected with COX8GFP. All transfections follow lipofectamine 3000 protocol.

2.3.2 Artificial mitochondria isolation

Mitochondria were isolated using mitochondria isolation kit for cultured cells (89874 Thermo Fisher Scientific). MCF10As were cultured in T75 flasks for 3 days and acquired 5 x 10^6 cells before any labelling or treatment. Centrifugation works were done according to protocol in a 4^oc temperature cold room and other transportation process were done on ice. Mitochondrial protein concentration was measured by Bradford assay (23236 Thermo Fisher Scientific, USA) to quantify amount of isolated mitochondria per trial. The standard curve was referenced by bovine serum albumin (BSA, A7906 Sigma Aldrich, USA) at concentration of 0, 25, 125, 250, and 500 μg/mL diluted in DPBS (25-508 Genesee, USA). Absorbance at 560nm was done on a spectrophotometer Nanodrop 2000 (ND2000CLAPTOP Thermo Fisher Scientific, USA), at least 4 data points were done on each concentration to produce standard curve. Freshly isolated mitochondria were inserted to breast cancer cell (BCC) culture and incubated till fully consumed in host cells.

2.3.3 MitoMeter, mitochondrial dynamics analysis

Mitochondrial dynamics were analyzed through MitoMeter[44], an automated segmentation for tracking of single mitochondria, to support the changes of mitochondria metabolic state through their behaviors and morphology dynamics. All timelapse videos were acquired in the same parameters following 0.07μm pixel size, 512 x 512 frame size, 1 second interval, and 3 minutes

total time. Data analysis and image processing were performed on MATLAB 2022rB. Solidity is calculated by the ratio between true pixel area and total volume of convex hull which indicates the branching of mitochondrial network.

2.4 Results

2.4.1 Cell co-culture and centrifuge extraction

Following Ivers *et al.* works[44] in co-culturing two different cell lines to trigger mitochondria transfer, we labelled healthy epithelial cell line MCF10A and BCC mitochondria by staining it with MitoTracker Green and Deep red respectively and co-cultured under cell sustainable condition for over 24 hours (Fig. 2.1 a). The analysis of the co-cultured image revealed the initial exchange of epithelial mitochondria in BCCs, which was indicated by punctuated green dots. However, other cells that express of both colors did not help differentiate between cell types and posed a risk of probe diffusion in between cell co-culture.

To validate the uptake from epithelial cells and the direction of mitochondria transfer, COX8GFP labeled mammalian cell mitochondria were artificially isolated and fed to stable expressing mCherry BCC culture. The resulting analysis confirmed the transfer of epithelial mitochondria in the BCCs, as indicated by the extension of COX8GFP signal to a mitochondrial network. Moreover, the presence of TNT-like structures between BCCs containing transferred mitochondria suggested that BCCs can also export mitochondria. To

further investigate the fusion of exogenous and endogenous mitochondria, BCC mitochondria were labeled by transfecting Mito7-mRuby, which revealed the entering of epithelial mitochondria after 12 hours and the fusion of two sources after 24 hours of incubation time (Fig. 2.1 b,c,d,e,f,g). However, this finding necessitated the analysis of single mitochondrial dynamics as they were neither original nor transferred mitochondria anymore which will be discussed in the next chapter.

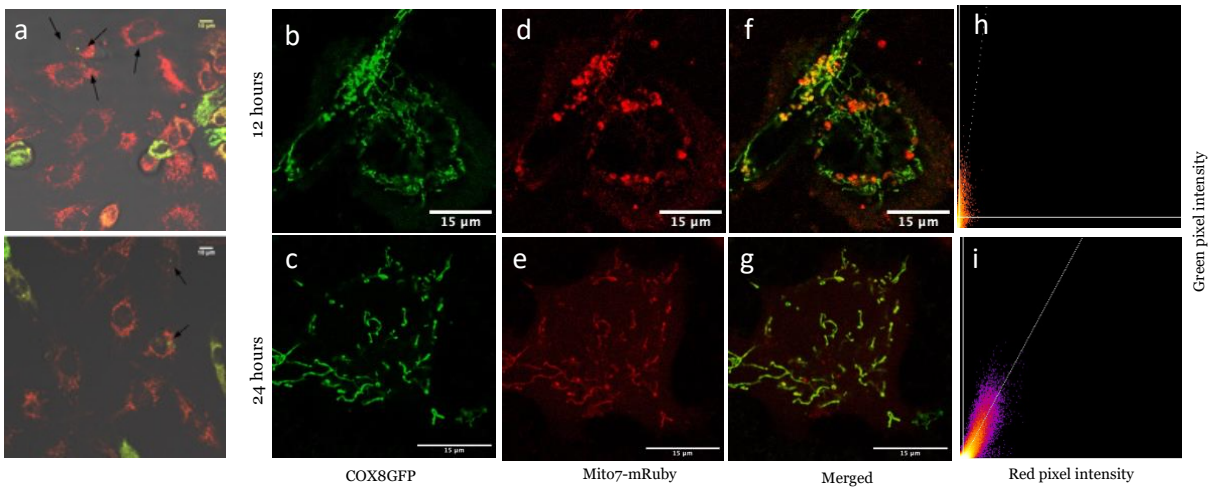

Figure 2. 1 Fluorescence images of coculture and artificial isolated mitochondria. a) Cocultured MCF10A and MDA-MB-231 in 4:1 ratio. Green dots of MCF10A mitochondria were found in deep red mitochondria cell body while fully overlapping cells may refer to transferred mitochondria dominating recipient cells but could also be due to diffusion of protein labeled dyes. b,c) endogenous and d,e) exogenous mitochondria in post 12 hours and 24 hours incubation. h,i) Colocalization scatter plots were calculated through e) merged images presenting Pearson's R of 0.59 and 0.72 in post 12 hours and 24 hours incubation respectively. Costes randomization value: 10, *p*-value = 1 (Significant of colocalization > 0.95).

2.4.2 Mitochondrial dynamics analysis

MitoMeter, an automated tracking algorithm for mitochondria in live-cell time-lapse images, was applied to analyze dynamic cues of morphology after uptake of epithelial mitochondria. Fig. 2.2 a shows the solidity of single mitochondria in timelapse videos which represents the

branching of mitochondrial network. The present study demonstrates a decrease in Solidity subsequent to the internalization of epithelial mitochondria in BCCs. These findings provide supportive evidence for our hypothesis that exogenous mitochondria augment the respiratory function of host cells. Oligomycin was induced to BCCs to test for positive control of fission events as shown in Fig. 2.2 a, Fig. 2.2 d, and Fig. 2.2 e where solidity increased due to the round shaped morphology of mitochondria undergoing fission as well as the decreasing major axis length being measured and compared with control. Notably, transferred mitochondria was found to have the same affects with Ruxolitinib (Rub), a JAK 1/2 inhibitor that kills tumor cells through toxic mitophagy. The shortening of major axis length but increase of branching may imply that mitochondria transfer regains selectivity of dysfunction mitochondria through mitophagy. An additional noteworthy observation is the heightened mitochondrial content in both BCCs, indicating the occurrence of mitochondrial biogenesis. This phenomenon entails the stimulation of cells to acquire greater mitochondrial metabolic capacity, further substantiating our proposed hypothesis regarding the augmentation of Oxidative Phosphorylation.

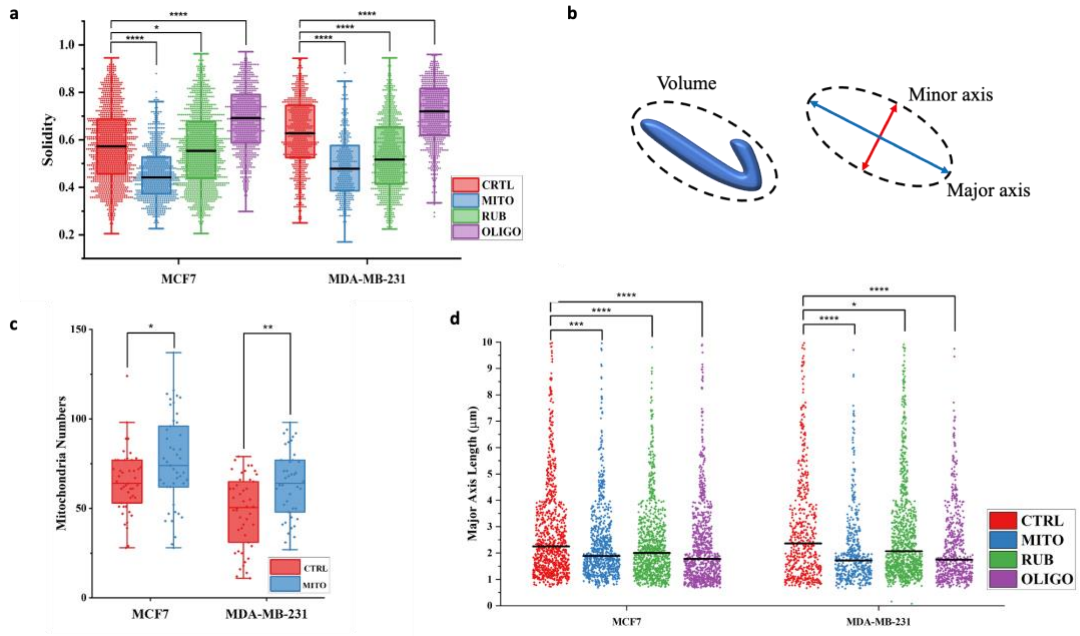

Figure 2. 2 MitoMeter analysis of mitochondrial dynamics. a) Solidity of BCCs treated with epithelial mitochondria, mitophagy activator Ruxolitinib, and fission activator Oligomycin respectively. Data are represented as mean ± interquartile ranges. p-values are calculated using two sample Kolmogorov-Smirnov test. * indicates $p < 0.05$ and **** indicates $p < 0.00001$. b) Solidity is represented by the ratio of true object pixels to the convex hull (volume) which indicates the branching of mitochondria network. Object and track numbers represent individual mitochondria numbers. Mitochondrial length is calculated by the ratio of major and minor axis length. c) Mitochondrial numbers before and after transferred mitochondria post 24 hours incubation. Data are represented as mean ± interquartile ranges. p-values are calculated using pair sample t test. * indicates $p < 0.05$ and ** indicates $p < 0.001$. d,e) Mitochondrial length of BCCs treated with epithelial mitochondria, mitophagy activator Ruxolitinib, and fission activator Oligomycin respectively.

MitoMeter not only analyzes mitochondrial dynamics in 2D but also 3D sliced time lapse images which is beneficial to mimic tumor microenvironment. However, confocal microscope setups limit penetration depth of focal point at ~2μm which is inadequate if were to image samples in 3D or spheroid/organoid models. The side-SPIM system creates light sheet excitation to acquire 3D images with minimal phototoxicity (Fig. 2.3). This will be discussed in Chapter 5 for more applications and introduction to the system.

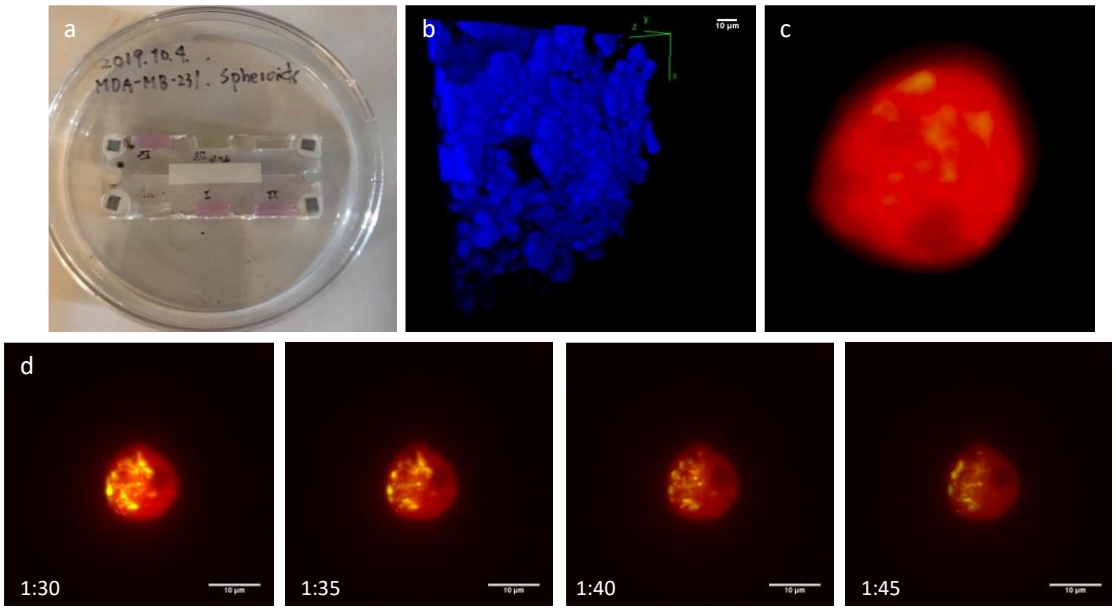

Figure 2. 3 Side-SPIM imaging of breast cancer spheroid. a) 300nm diameter spheroids were cultured in 96 well plates and later transported to specialized window chambers. b) Peripheral 3D image of spheroid stained with NucBlue c) 3D sliced image (z = 14µm) of mCherry MDA-MB-231 containing transferred mitochondria expressing COX8GFP. d) 15 seconds timelapse images of mitochondrial movement inside recipient cell.

2.4.3 Cell viability and drug sensitivity

To investigate the impact of epithelial mitochondria on BCC cell death, a cell viability assay was performed on BCCs treated with the anti-cancer drug, Doxorubicin, at varying concentrations (Fig. 2.4). The results of the assay revealed that the cell proliferation of BCCs containing epithelial mitochondria was enhanced, but concurrently, these cells became more sensitive to drug treatments. This outcome was anticipated given the observed fusion of transferred mitochondria with endogenous mitochondria, thereby re-establishing normal mitochondrial function and consequently losing tolerance to high levels of oxidative stress. Moreover, the combination of transferred mitochondria and Doxorubicin was observed to

result in more cell death than metabolic inhibitors (Supplement). This discovery highlights the potential of mitochondria transfer in therapy, as it enhances sensitivity to anti-cancer drugs.

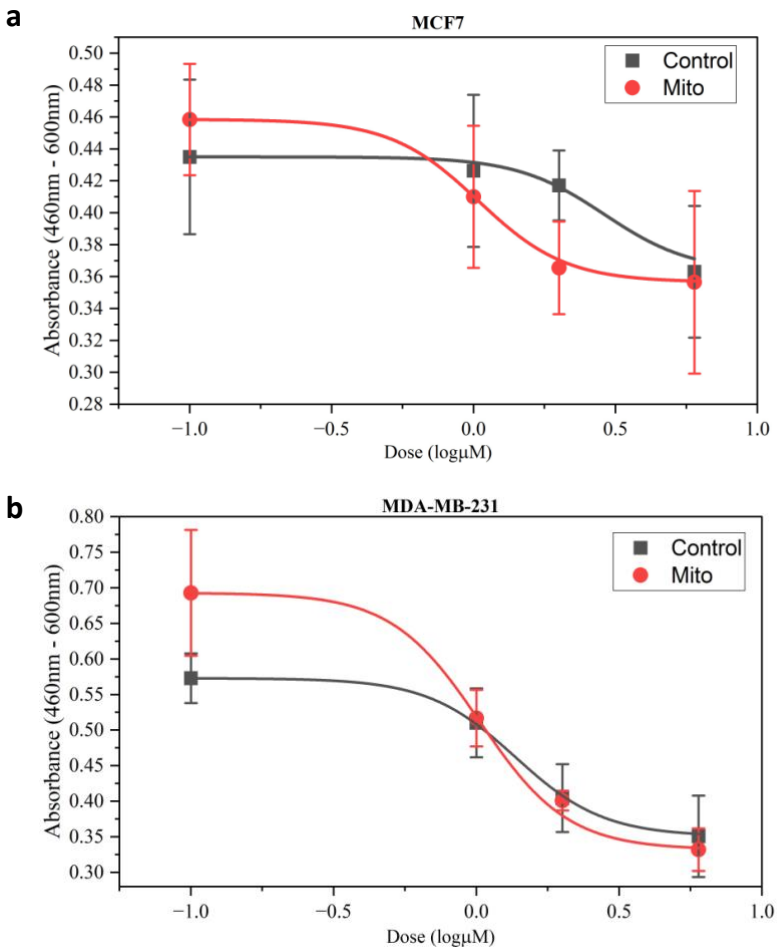

Figure 2. 4 Cell viability of BCCs exposed to Doxorubicin. Dosage curve was produced by XTT assay absorbance of a) MCF7 and b) MDA-MB-231 cells treated with 0, 1, 2, and 5 μM of Doxorubicin after 3 days performed by XTT assay.

2.5 Discussion

The validation of mitochondria transfer was done via fluorescence confocal microscopy images. In our experiments, the transfer rate of mitochondria worked better in artificial isolation than co-culturing two cell lines together, hence the transferred mitochondria samples later mentioned in this thesis are all referred to artificially isolated mitochondria. Interestingly, TNT-

like structures were discovered containing transferred mitochondria in between MCF7 cells. This suggests that BCCs do not simply uptake mitochondria through endocytosis but also interacts between cell bodies knowing that MCF7 morphology are normally aggregating and attached instead of connecting through TNTs. MitoMeter results suggest the shifting of metabolism where increase of branching and numbers of mitochondria both indicated the occurrence of mitochondrial biogenesis. This raised the need to investigate metabolic state of these newly formed mitochondria product which will be discussed in the next chapter. Moreover, although transferred mitochondria were found to favor breast cancer cell growth, the host cells may have lowered tolerance of oxidative stress level since they became more sensitive to Doxorubicin. This encourages epithelial mitochondria transfer to be considered once again to eliminate cancer cells.

CHAPTER 3. PHASOR APPROACH TO FLIM OF SINGLE MITOCHONDRIAL NADH

3.1 Abstract

Bulk metabolic assays on cell populations have shown that mitochondria transfer trigger breast cancer cells turn towards Oxidative Phosphorylation (OXPHOS) in favor of proliferation, migration, and cell growth. Yet, the current methods lack single cell resolution of interaction between endogenous and exogenous mitochondria to help understand the consequence metabolic alterations and other cell fate decisions. The phasor approach to Fluorescence Lifetime Imaging Microscopy (FLIM) has been widely used to measure the free to bound fraction of reduced form of NADH to quantify metabolic changes in live cells but not at the single mitochondrial scale. Here, we developed the FLIM intensity-based image segmentation (FIBIS) algorithm as a robust approach to recognize mitochondria from NADH intensity and further analyze mitochondrial metabolic states to investigate effects of mitochondria transfer. This chapter demonstrates that the NADH autofluorescence perfectly localizes with Mito7-mRuby labeled mitochondria and is free from artifactual emission spectral overlaps. Our data indicates that there was a 40% and a 20% increased fraction of bound NADH after mitochondria transfer in MCF7 and MB231 cells, respectively. This suggests that there is an enhancement of OXPHOS for both breast cancer cells. This was in correlation with the results from the Seahorse XF analyzer where the oxygen consumption rate was significantly higher

after uptake of isolated mitochondria from breast epithelial cells. We also used Mitometer to show that there were increasing numbers of mitochondria and branching which imply that the fusion of exogenous and endogenous mitochondria are highly adaptable and increase cellular respiration. In summary, the FLIM intensity-based image segmentation method enables single mitochondrial metabolic profiling and aids in understanding the effects of transferred mitochondria to recipient cells. Our results also indicate that transferred mitochondria in cancer cells enhances OXPHOS, increased branching, and mitochondrial numbers thereby decreases cell viability and increases sensitivity to chemotherapy agents.

3.2 Introduction

Metabolism[45] refers to the complex network of chemical reactions that occur within cells, tissues, and organisms to sustain life. The metabolism of a cell refers to the balance between anabolic and catabolic processes, which are responsible for the synthesis and breakdown of molecules, respectively. In general, cells exist in two types of metabolism: anabolism or catabolism. In an anabolic state, cells use energy to synthesize molecules, such as proteins, nucleic acids, and lipids. Anabolism is essential for growth, repair, and maintenance of cellular structures and functions. In a catabolic state, cells break down molecules to release energy, which can be used for cellular processes such as ATP production or biosynthesis. Catabolism

is essential for providing energy to sustain cellular functions and maintain homeostasis which is also referred as cellular respiratory.

Cancer cells have altered metabolism compared to normal cells, and one of the key features of this altered metabolism is increased catabolism. For cancer cells to support their rapid growth and proliferation, they often rely on catabolism to break down molecules such as glucose, fatty acids, and amino acids to generate energy and building blocks for macromolecules such as nucleic acids and proteins. Furthermore, many cancer cells have increased glycolysis and reduced mitochondrial respiration, a phenomenon known as the Warburg effect[46]. This altered metabolism allows cancer cells to rapidly generate ATP and biomass, which stands a critical break point in between cancer and normal cells. In this chapter, the consumption of transferred mitochondria alters the metabolism again in host cancer cells that may favor the proliferation, energy production, and migration rate.

The following three methods were applied to measure the altered metabolism caused by mitochondria transfer: Seahorse assay, mitochondrial membrane potential, and the phasor approach to FLIM. Briefly introduce seahorse assay, mitochondrial membrane potential, and phasor approach to FLIM. Seahorse assay[47] is a method used to measure the rates of glycolysis and oxidative phosphorylation. It involves using a specialized instrument called a Seahorse analyzer, which measures the extracellular acidification rate (a measure of glycolysis) and the oxygen consumption rate (a measure of oxidative phosphorylation) of cells in real time.

Another method called mitochondrial membrane potential[48], measures the electrical potential difference across the inner mitochondrial membrane, which is generated by the proton gradient established during oxidative phosphorylation. This potential difference is critical for mitochondrial function, as it drives the synthesis of ATP, the energy currency of the cell. Finally, the phasor approach to FLIM[49] measures the lifetime intracellular metabolic co-factor, NADH, to imply the metabolic state of, in this thesis work, single mitochondria. The findings presented in this chapter demonstrate that the phasor approach to Fluorescence Lifetime Imaging Microscopy (FLIM) yields valuable insights beyond metabolic profiling of individual mitochondria. Specifically, we show that by utilizing the FLIM intensity-based image segmentation (FIBIS) algorithm, we are able to identify the location of single mitochondria based on their NADH autofluorescence intensity, and thereby obtain both morphological and metabolic information from segmented FLIM images. This approach not only enables visualization of mitochondrial dynamics, but also allows for quantification of metabolic states in individual mitochondria, providing a powerful tool for tracking the fate of newly formed mitochondria. Overall, our results demonstrate the potential of the phasor approach and FIBIS algorithm for advancing our understanding of mitochondrial function and dynamics.

3.3 Material and Methods

3.3.1 Fluorescence Lifetime Imaging Microscopy (FLIM)

When electrons of a fluorescent probe or a fluorophore are stimulated from ground state, S0, to excited state S1 or S2, the energy which drops back to ground state emits a photon and produces the phenomenon called fluorescence. The process of fluorescence could be explained by the Jablonski diagram[50] (Fig. 3.1). The average time a fluorophore spends in the excited state before emitting a photon and returning to the ground state is hence defined as the fluorescence lifetime. Fluorescence lifetime is generally within the range from picoseconds to hundreds of nanoseconds and is scarcely interfered by environmental or concentration issues except for temperature and the presence of fluorescence quenchers. This makes fluorescence lifetime a sensitive and accurate method to measure fluorophore property, environmental changes, and protein interaction.

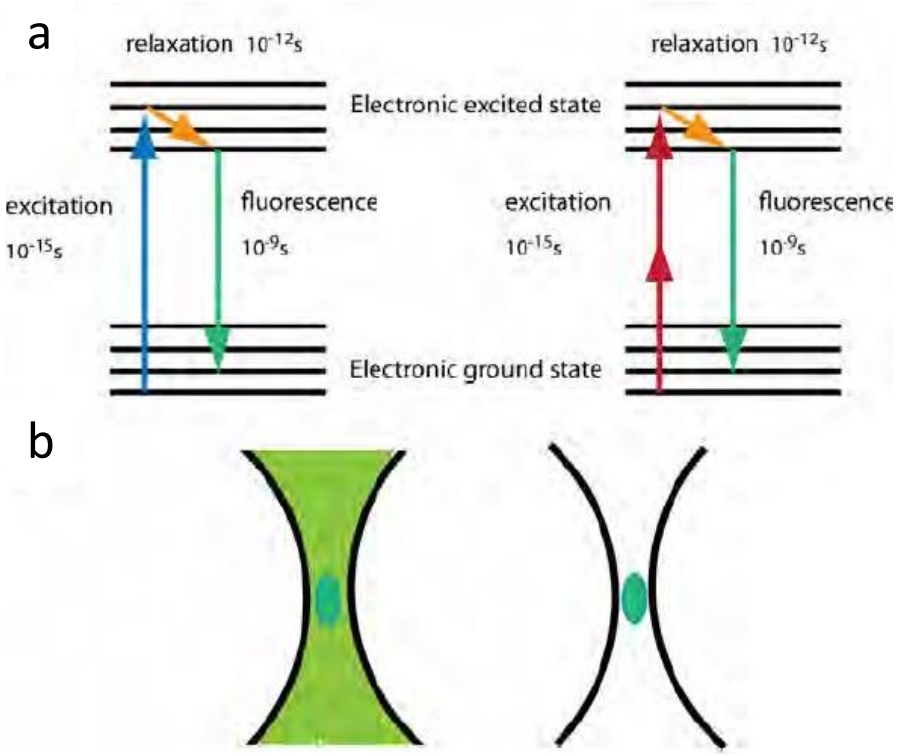

Figure 3. 1 Jablonski diagram for one-photon and two-photon excitation. Note that two photon has a more confined focal region than one photon excitation allowing all fluorescence photon generated at the point which benefits the penetration when imaging thick samples. Figure from Chen (2012). Reprint with permission from intechopen.

To acquire fluorescence lifetime data, hardware approaches can be separated into two parts, time and frequency domain. In the **time domain** FLIM, fluorophores are excited by an extremely narrow pulse of light source in order to prevent other excitation during molecule decay. The detectors (photomultiplier tubes or avalanche photodiodes) capture the excited photons and then sent to gated recorders (time-correlated single photon counting or fastFLIM box) accumulating their arrival times to build up fluorescence decay curve. The distribution of curve histogram can be described in the following equation:

$$I_{(t)} = I_0 e^{-\frac{t}{\tau}}$$

Where I is the fluorescence intensity, I_0 is the fluorescence intensity at initial time, τ is the lifetime, and t is the time delay after excitation pulse. A mono-exponential decay fits the fluorescence lifetime of a single fluorophore. However, live cell environments contain of various fluorophores which produces multi-exponential decay that is described in the following equation:

$$I_{(t)} = \sum_i \alpha_i e^{-\frac{t}{\tau}}$$

Where i is the component index and α is the pre-exponential factor. This requires of heavy mathematical deconvolution to resolve number of fluorophore components.

In the **frequency domain** FLIM, the excitation light source is sinusoidally modulated at high frequencies as in the following equation:

$$E_{(t)} = E_0(1 + M_{ex}\sin(\omega t))$$

Where $E_{(t)}$ is the excitation intensity at time t, E_0 is the initial excitation intensity, M_{ex} is the excitation modulation factor, and ω is the angular modulation frequency of the excitation light source. This modulated light source gives emission to the fluorophore and produces another modulated emission as described in the following equation:

$$F_{(t)} = F_0(1 + M_{em}\sin(\omega t + \varphi))$$

Where $F_{(t)}$ is the emission intensity at time t, F_0 is the initial emission intensity, M_{em} is the emission modulation factor, ω is the angular modulation frequency of the excitation light source, and φ is the phase delay of emission sinusoidal wave.

Fluorescence lifetime can be determined from both the reduction of emission intensity and phase delay as described in the following equation:

$$M = \frac{1}{\sqrt{1+(\omega\tau_m)^2}}$$

$$\omega = \tau_p \tan(\varphi)$$

Where M is the amplitude reduction (demodulation), which is the ratio between emission and excitation modulation, ω is the angular modulation frequency of the excitation light source, and φ is the phase delay of emission sinusoidal wave. τ_m and τ_p is the lifetime derived from magnitude reduction and phase delay respectively. M is calculated from the AC and DC component ratio of their modulation as described in the following equation:

$$M = \frac{M_{em}}{M_{ex}}$$

$$M_{em} = \frac{AC_{em}}{DC_{em}}$$

$$M_{ex} = \frac{AC_{ex}}{DC_{ex}}$$

Although the approach to acquire lifetime is different between time and frequency domain, the data are mathematically equivalent and can be interconverted by Fourier transform.

3.3.2 The Phasor Approach to FLIM

As mentioned in multiexponential decay for lifetime determination, it takes heavy math to curve fit for different fluorophores and is not directly quantifying their individual contribution

to the histogram. In order to better visualize and analyze multiple lifetime contribution, the phasor approach transforms the fluorescence decay (from time domain) or maps the phase delay and modulation (from frequency domain) into a new coordinate system called the phasor plot. This allows the determining of fluorophore lifetime free from fitting and also provides graphical results making it convenient for quantification. The phasor approach to FLIM was first introduced by Weber[51] and soon developed into graphical analysis by Jameson[52]. The coordinates of phasor plot were transformed from time domain data using the following equations:

$$g_{i,j}(\omega) = \frac{\int_0^T I_{i,j}(t)\cos(\omega t)\,dt}{\int_0^T I_{i,j}(t)dt}$$

$$s_{i,j}(\omega) = \frac{\int_0^T I_{i,j}(t)\sin(\omega t)\,dt}{\int_0^T I_{i,j}(t)dt}$$

Where $g_{i,j}(\omega)$ and $s_{i,j}(\omega)$ are the phasor coordinates of pixel location (i,j), ω is the angular modular frequency of excitation light source, T is the gating time of fluorescence decay histogram, and $I_{i,j}(t)$ is the intensity of pixel location (i,j) at time t. The coordinates of phasor plot that were transformed from frequency domain uses the following equations:

$$g_{i,j}(\omega) = M_{i,j}\cos(\varphi_{i,j})$$

$$s_{i,j}(\omega) = M_{i,j}\sin(\varphi_{i,j})$$

Where $M_{i,j}$ is the modulation and $\varphi_{i,j}$ is the phase delay at pixel location (i,j).

By the equations mentioned above, the phasor plot is presented as a semi-circle which centers at (0.5,0). At a lifetime of zero, the phasor position is at (1,0) and the single exponential lifetime decay increases along the semi-circle and lands at (0,0) which stands for infinite lifetime. Notably, the phasor plot of multi-components lifetime distributes within the semi-circle which is generated by the components' contribution. This is an important concept to quantify the free and bund fraction of NADH being mentioned below, where the distribution of phasors indicates the contribution of their individual lifetime and draws out the metabolic trajectory shown in Fig. 3.2.

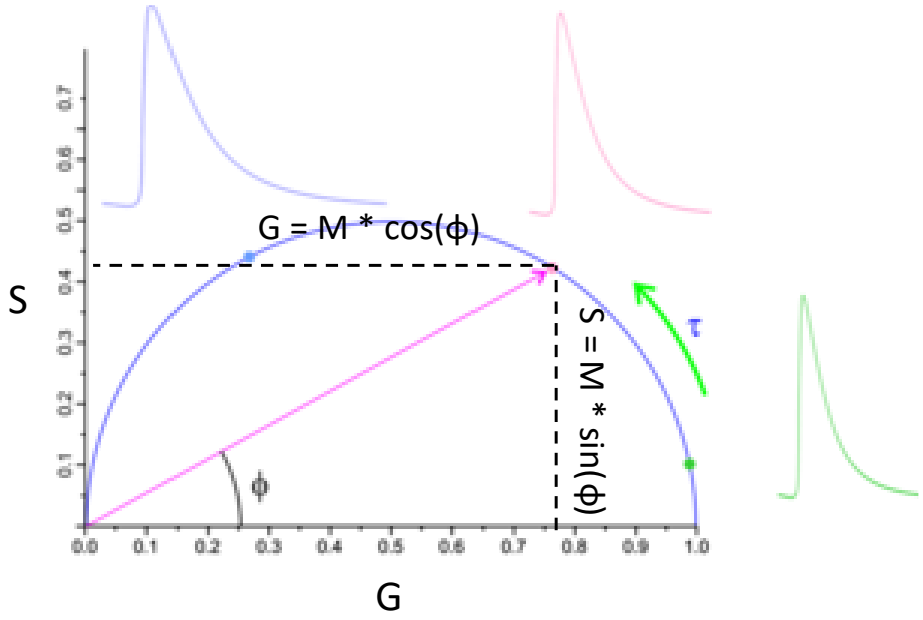

Figure 3. 2 Phasor plot. Photon arrival time forms exponential decay in the time domain which are then Fourier transformed into the frequency domain of (G,S) coordinates. Figure from https://en.wikipedia.org/wiki/Phasor_approach_to_fluorescence_lifetime_and_spectral_imaging

3.3.3 NADH FLIM

The reduced form of nicotinamide adenine dinucleotide (NADH) is an important co-factor in the cell metabolism pathway[53]. It is mainly used to manage electron availability in both glycolysis and oxidative phosphorylation (OXPHOS). In glycolysis, NAD is reduced to NADH during glucose transition to pyruvate and enter the tricarboxylic acid cycle (TCA cycle) in the mitochondria. In OXPHOS, NADH is mainly bound to complex I and oxidized back to NAD in the electron chain to charge electron gradient between mitochondria matrix and intermembrane space for ATP production.

Current methods use NADH/NAD+ ratio to differentiate between cellular metabolic states in the single cell level[16]. However, utilizing the lifetime characteristic is relatively more stable and accurate since it is an intrinsic auto-fluorophore which does not require additional staining or labelling. While NADH has a wide emission spectrum from 420 – 550 nm and a relatively low quantum yield (0.02), two photon excitation at 720-740 nm wavelength can increase fluorescence intensity and the use of bandpass filter 460/80 nm can capture NADH emission but avoid shorter peak emission wavelengths of collagen and elastin.

When binding to proteins, the conformation of NADH changes from the free state. Free state NADH presents a closed conformation where part of the excited adenine moiety is transferred to the dihydronicotinamide moiety, adding a quenching- based decay component, and increasing the overall fluorescence decay lifetime[54]. In bound state NADH, the molecule

unfolds and separates the adenine and dihydronicotinamide moieties, and thus the molecule's fluorescence lifetime is less affected by quenching and increases in decay time. The relatively large difference between bound state NADH (~3.4 nsec) and free state NADH (0.4 nsec) lifetime makes a linear relation on the phasor plot. The metabolic profiling of single cell or, in this work, mitochondria is based on the fraction of the two extreme points.

3.3.4 FLIM intensity-based image segmentation

Apart from phasor transformation, intensity (I) of NADH was collected depending on photon counts into our external photomultiplier tubes (PMT). Yet, the motion blur caused by mitochondria movement and unexpected high intensity pixels (Fig. 3.4 a) are the two major problems for our image segmentation method. Pixel intensities were auto scaled at current frame but eventually summed in one I array. We developed a MATLAB program, FLIM intensity-based image segmentation (FIBIS), to overcome difficulties mentioned above in a structured function shown in Fig 3.3.

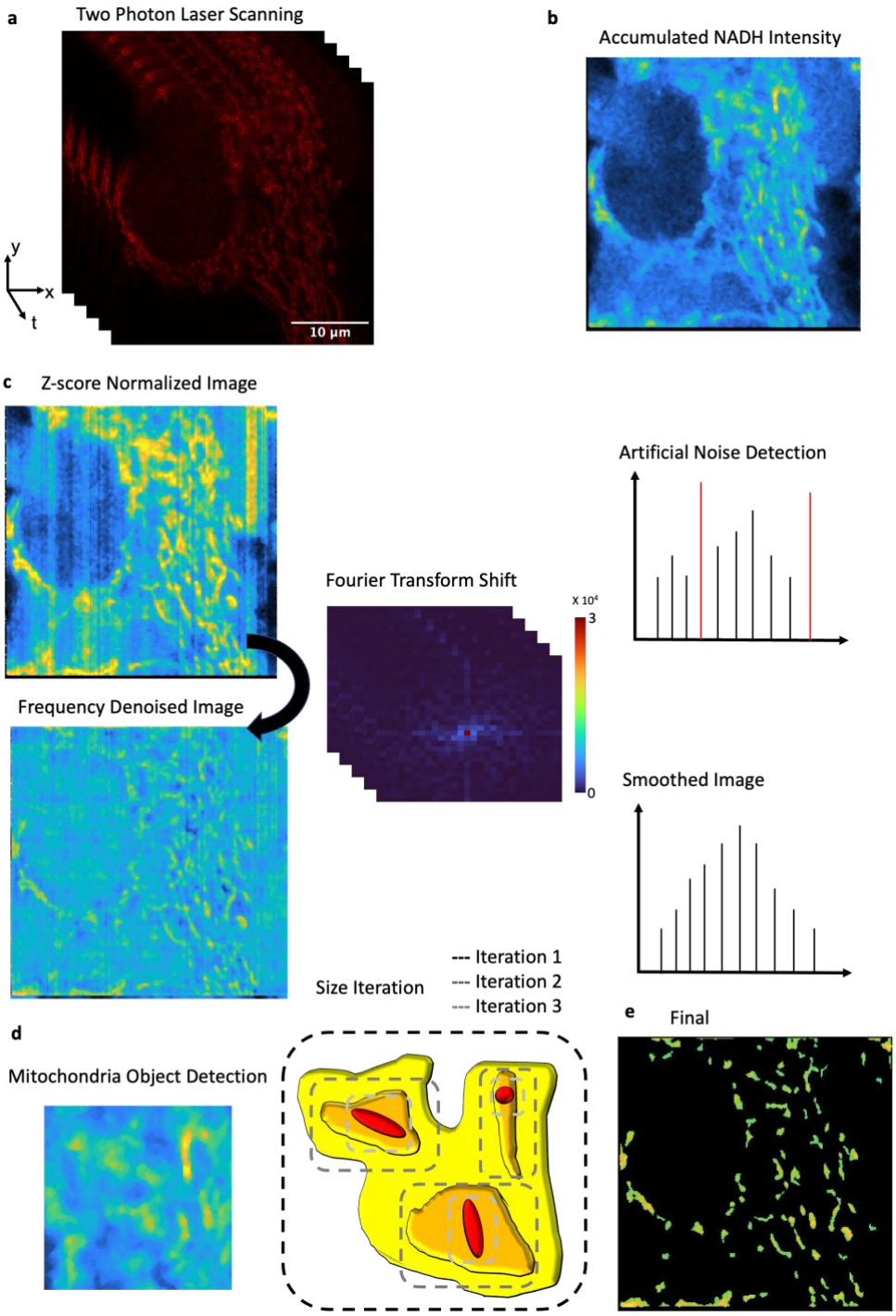

Figure 3. 3 Flowchart and MATLAB program structure of FIBIS. a) Images were line scanned by two photon laser excitation of 15 frames in total to collect sufficient photon arrival time resulting in b) accumulated intensity image. c) Highlight pixels were z-score normalized which amplified artificial laser scanning noise. FIBIS detects artificial noise through histogram abnormal peaks and determines optimal frequency smoothing from Fourier transform shift to set up threshold level. d) Objects that are larger than predefined size goes through size iteration following intensity gradient and ends up in e) final masked image.

We first range normalized I and amplified all NADH signature, including artificial frequency noise of laser scanning across field of view (Fig. 3.4 b) especially at two ends of image, where line scanning starts and ends (Fig. 3.4 f). To identify whether frequency noise was overwhelming, we performed local peak detection across the image histogram and found numerous peaks at various intensities (Fig. 3.4 d). Once frequency noise damages the histogram of I array, we performed Fourier transform shift and set threshold to pick out the frequency peak (Fig. 3.4 c) causing the majority of noise. Otsu threshold can then be set after smoothing peaks of the image histogram (Fig. 3.4 e) at 0.9 quantile. After initial masking of objects, we determine the size of mitochondria by the area property. This step is crucial to 1) clear remaining noise pixels and 2) reiterate large blobs for erosion method. Erosion method is applied to resolve dense distributed and locally moved mitochondria. Starting from size 8 strel, only relatively high intensity pixels were preserved for final masking of selected objects. The flow chart of NADH FIBIS method is aimed to create optimized thresholding histogram to preserve NADH signature and determine correct mitochondrial size to avoid motion blur recognized objects.

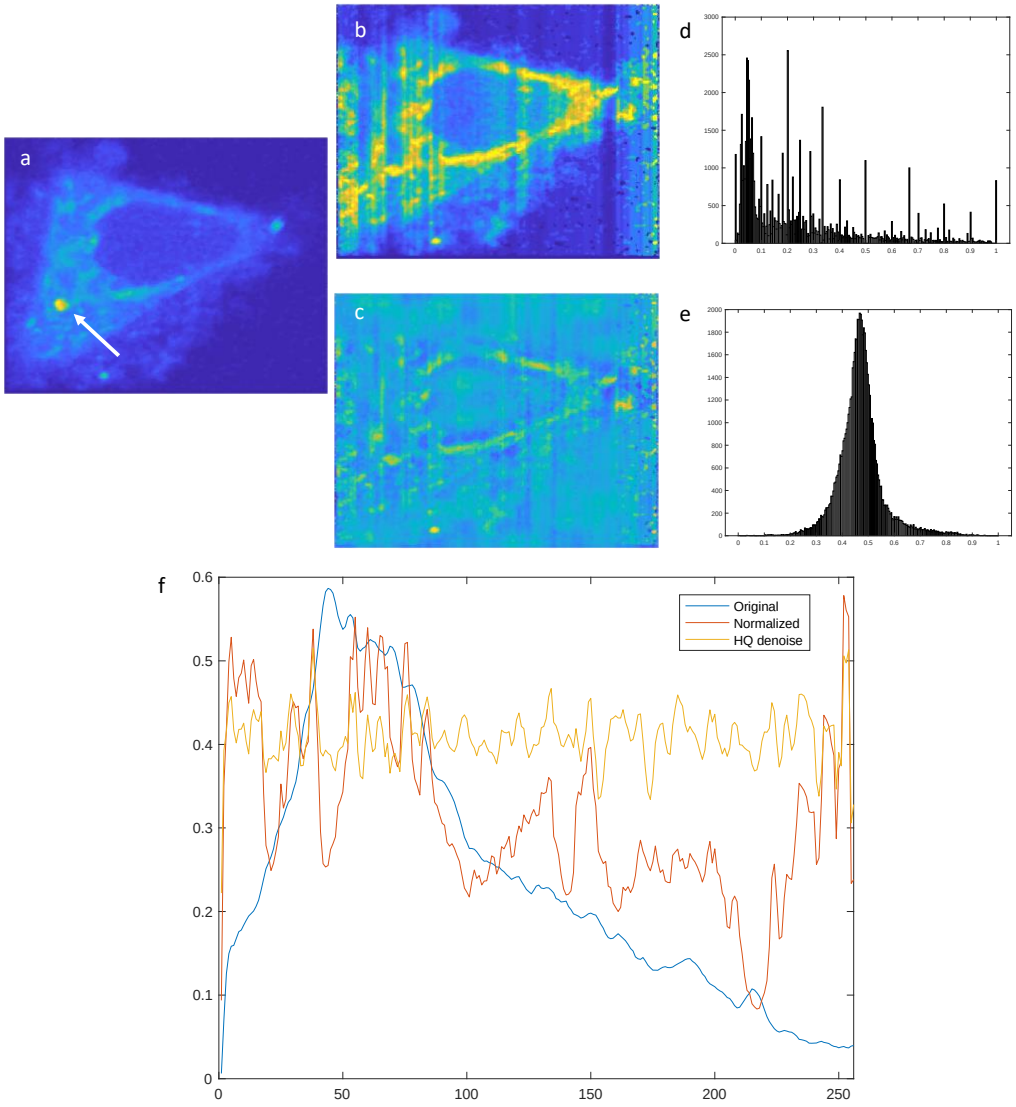

Figure 3. 4 Image processing of FIBIS. a) Raw intensity image of MCF7 cell where arrow pointed is the area of unexpected high intensity area decreasing other NADH signatures of the cell. b) Range normalized image which highlights whole frames NADH signature also containing of high frequency noise detected in local peaks of histogram d). c) Denoise filtered image exhibiting normal distributed histogram for thresholding e). f) Column averaged intensity of the 3 intensity images. Original curve showed the largest peak around the high intensity area. Normalized curve showed frequency noise across normalized image. HQ denoise has smoothed intensity but preserves NADH signature.

3.3.5 Seahorse XF analyzer

To validate the true metabolic data significance, we applied the Agilent Seahorse XF real-time analyzer to measure the flux of oxygen, the oxygen consumption rate (OCR), and the flux of

protons, the extracellular acidification rate (ECAR) as they represent the key parameters of cell metabolism. Notably, the instrument we use for this work is a Seahorse XFé24 analyzer which is customed to 24 well plate measurement. Each well is seeded with 10,000 – 12,000 cell density and changed to assay medium before measurement. The catridge was calibrated in a non-CO_2 incubator with calibrant media (103680-100 Agilent, USA), specifically for ECAR, 12 hours before measurement. 24 well plate was calibrated in a symmetry pattern for background calculation. During glycolysis, ATP production does not require oxygen and produces H+ and lactate which is shown in the chemical equation:

Glucose + 2 ADP + 2 Pi = 2 Lactate + 2 ATP + 2 H_2O + 2 H+

Where H+ correlates 1:1 with lactate accumulation indicating glycolytic rate. The pH-sensitive fluorophores are embedded in the sensor cartridges and are used to measure the changes in pH in the medium surrounding the cells. The fluorophore consists of a dye that changes color in response to changes in pH. The Seahorse XF analyzer uses light at a specific wavelength to excite the dye and measures the intensity of the emitted light at a longer wavelength to determine the pH of the medium. The proton efflux is measured at pmol/min unit.

During OXPHOS, oxygen is taken up in mitochondrial complex IV in part of the electron chain transport and turned into H_2O. The oxygen-sensitive fluorescence probes are embedded in the sensor cartridges and are used to measure the changes in oxygen concentration in the medium surrounding the cells. The probe consists of a phosphorescent dye that is excited by light at a

specific wavelength and emits light at a longer wavelength when exposed to oxygen. The intensity of the emitted light is proportional to the concentration of oxygen in the medium and is measured by the instrument's detector.

3.4 Results

3.4.1 Cellular free and bound fraction NADH by simFCS

The phasor approach to FLIM is analyzed through a software developed in the Laboratory for Fluorescence Dynamics, simFCS[55]. It calculates the phasor of each pixel from FLIM image after calibrated with strong and stable lifetime fluorophores such as Coumarine or Rhodamine. Free and bound fraction of NADH was analyzed by placing the cursors on two extreme points of the phasor distribution (Fig. 3.5 b) and create a linear scaled pseudo color bar (Fig. 3.5 c). In this study, stable expression of mCherry MDA-MB-231s with additional epithelial mitochondria (Fig. 3.5 a) was used as the sample group to produce a phasor plot. The results indicated a significant increase of bound NADH in the sample group compared to the control group (Fig. 3.5 d), confirming our assumption that transferred mitochondria can alter the host cancer cells to a more oxidative phosphorylation (OXPHOS) state. Notably, we were able to differentiate between exogenous and endogenous mitochondria using the two extreme cursors. Only exogenous mitochondria labeled with COX8GFP were highlighted, and none were found

in control images. This observation is promising for the development of single mitochondria segmentation based on NADH intensity and targeting their phasor signatures.

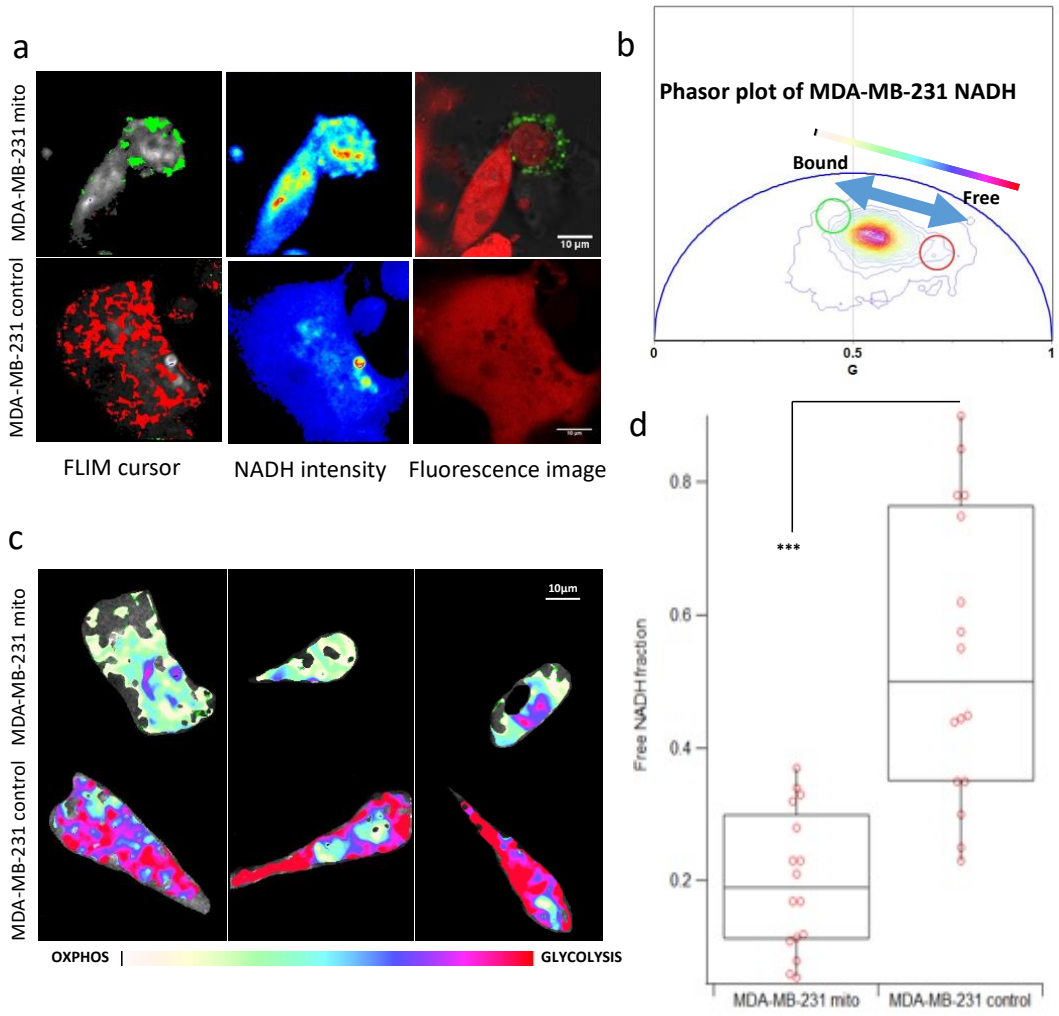

Figure 3. 5 simFCS analysis of single cellular metabolism. a) Stable mCherry MDA-MB-231 control and mitochondria group containing COX8GFP labeled mitochondria where green cursor pixels in b) phasor plot were overlayed with isolated mitochondria. c) Pseudo colored FLIM images showing metabolic shift of MDA-MB-231 towards OXPHOS after consuming isolated mitochondria and d) student t test of statistical significance. Data are represented as mean ± interquartile ranges. p-values are calculated using student t test. *** indicates $p < 0.0001$. $N = 20$.

3.4.2 Single mitochondria recognition by FLIM intensity-based image segmentation (FIBIS)

While the previous section has demonstrated the quantification of single cell level metabolic index, it fails to give information of individual mitochondria. To target only the mitochondrial NADH phasors, we developed the FIBIS method. FIBIS is based on the intensity of NADH auto-fluorescence to segment highlighted pixels targeting mitochondrial localization. Through the frames that are taken to collect sufficient photons for lifetime histogram, FIBIS normalizes total pixel intensities and denoise artificial frequencies caused by the laser line scanning throughout the field of view. This overcomes the two major problems when acquiring NADH FLIM images since 1. fast moving mitochondria have traveled across region of interest where the tracks created a motion blur in the final summed image (Fig 3.6 c) and 2. relatively high intensity pixels may diminish other NADH signature pixels which makes it difficult to determine optimized cutoff for image thresholding. To quantify optimization of FIBIS method, raw intensity and FIBIS images were compared with their corresponding Mito7-mRuby fluorescent labelled images as reference (Fig. 3.6 b) using Structural similarity (SSIM). The emission spectrum of NADH and mRuby were widely separated to prevent signal overlapping. FIBIS performed a better structure comparison than raw intensity overall in the 30 trials (Fig. 3.6 a) bringing a 35% increase in similarity test. In short, FIBIS method helps phasor FLIM

users to robustly crop and label individual mitochondria with their fraction index on free to bound NADH trajectory.

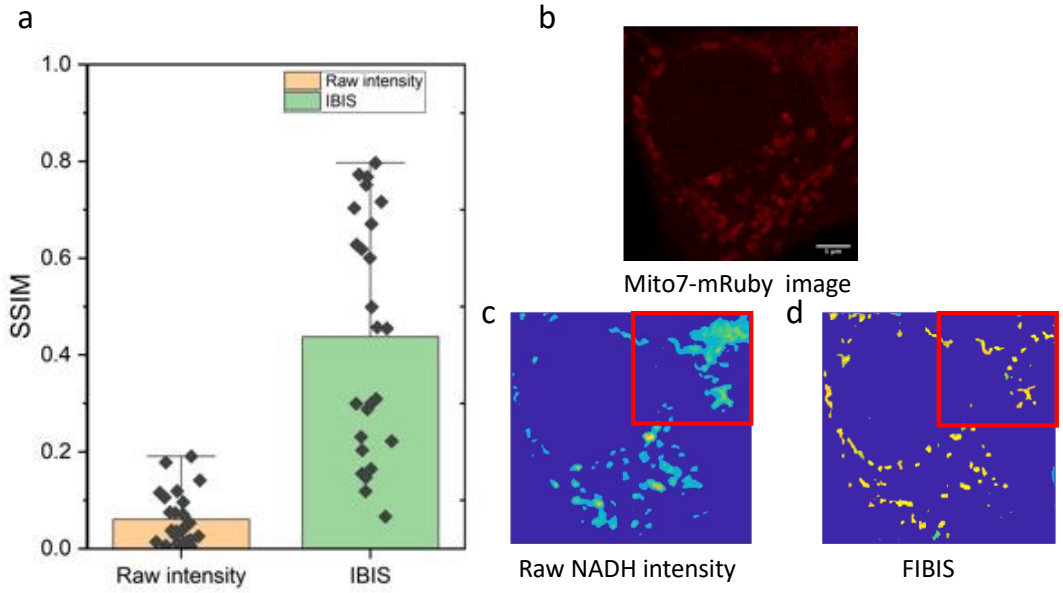

Figure 3. 6 Structural similarity test. a) FIBIS increased 35% of similarity referenced by b) Mito7-mRuby labeled mitochondria images compared to Otsu thresholding of raw intensity image. The highlighted area in c) represents mitochondrial motion blur due to scanning frames across time and where d) FIBIS was able to differentiate mitochondrial location by highlighting strong NADH autofluorescence signal.

3.4.3 Metabolism inhibition studies compared with mitochondria transfer

Healthy mitochondria transfer is assumed to help regain normal metabolic functions in breast cancer cells. To validate the assumption, we induced metabolic inhibitors to breast cancer cells and quantified the free and bound fraction NADH of individual mitochondria. The lifetime of 2.5µM NADH was measured to calibrate the pure population of unbound NADH in 10mM NaH_2PO_4 solution, Fig. S2 shows the single exponential lifetime at 0.4 nsec and ~3.5 nsec with pure mitochondria indicating bound NADH on the phasor plot. The free and bound fraction

(FB fraction) NADH FLIM analysis revealed an increase in the bound fraction NADH of 42% and 20% post 24 hours transferred mitochondria in both MCF7 and MDA-MB-231 cells respectively (Fig. 3.6 c,d). The increased bound NADH fraction is identical with BCCs treated with the glycolytic inhibitor, 2-deoxyglucose. This suggests that mitochondrial enhancement changes cellular respiration towards the OXPHOS state. Oppositely, fraction of bound NADH decreases when treated with OXPHOS inhibitor, Rotenone, which shows the ability of cancer cells to switch between metabolic states freely to meet self-growth (Fig. 3.6 a).

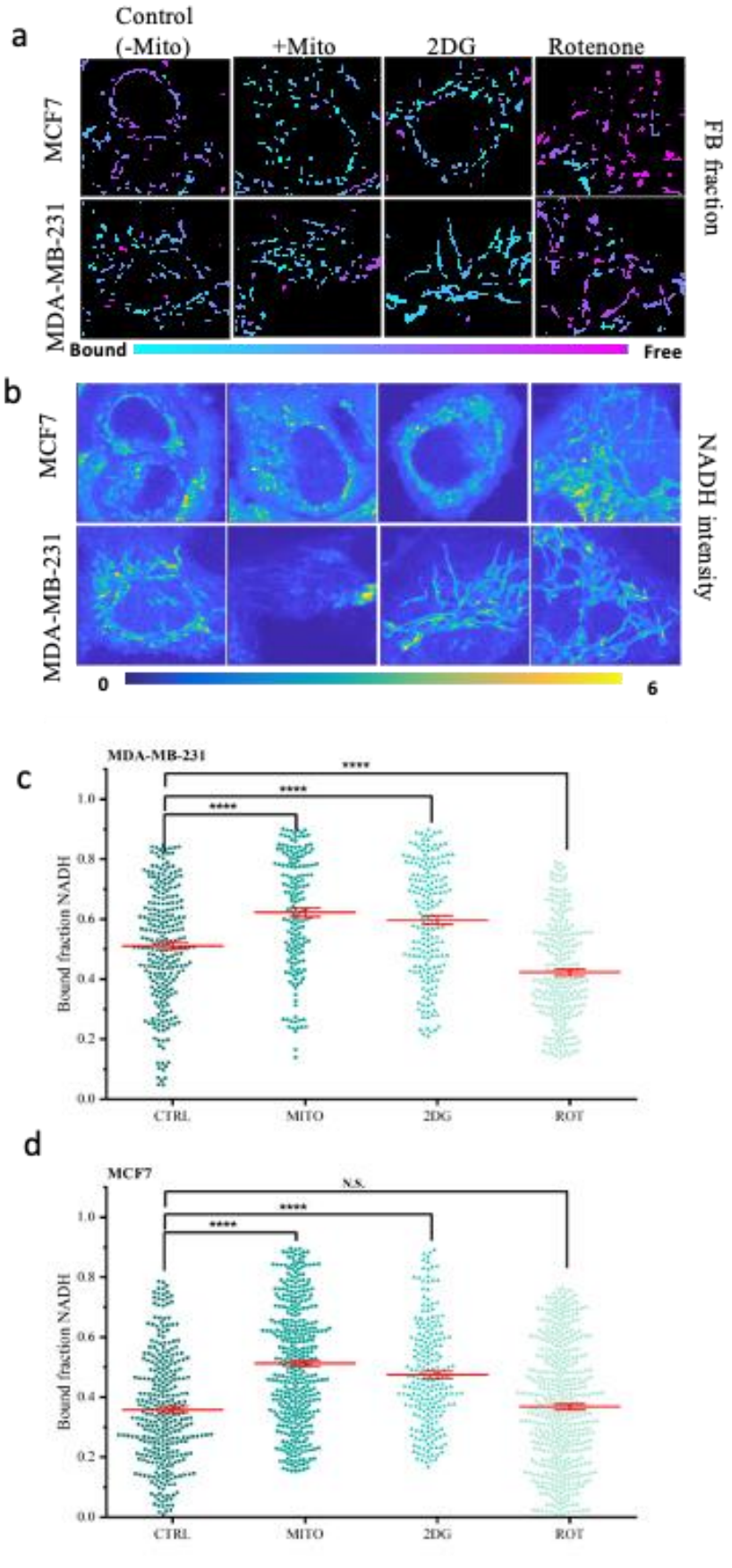
a
Control
(-Mito)
+Mito
2DG
Rotenone
MCF7
MDA-MB-231
FB fraction
Bound
Free
b
MCF7
MDA-MB-231
NADH intensity
0
6
c
MDA-MB-231
Bound fraction NADH
****
****
****
CTRL
MITO
2DG
ROT
d
MCF7
Bound fraction NADH
N.S.
****
****
CTRL
MITO
2DG
ROT

Figure 3. 7 FIBIS analysis of single mitochondria metabolic profiling. a) Segmented mitochondria overlaid with pseudocolor referenced from phasor plot free and bound fraction NADH. b) Raw NADH intensity images of BCCs. Scale bars, 10μm. Shown are selected images from BCCs under four different conditions. Scatter plot of segmented mitochondria FB fraction. n = 612, 490, 538, and 589 distinct mitochondria in c) MDA-MB-231 control, transferred mitochondria, 2-Deoxyglucose, and Rotenone respectively. n = 915, 765, 723, and 872 distinct mitochondria in d) MCF7 control, transferred mitochondria, 2-Deoxyglucose, and Rotenone respectively. p-values are calculated using two sample Kolmogorov-Smirnov test. N.S. indicates no significance and **** indicates $p < 0.00001$.

3.4.4 Measurement of oxygen proton flux: Seahorse XF analyzer

To compare our imaging results, we utilized the seahorse assay, the gold standard method for metabolic investigations, to measure the two breast cancer cell lines transferred with epithelial mitochondria. MCF7 with additional transferred mitochondria shows a significant increase in OCR and decrease in ECAR, implying the shift of metabolism towards OXPHOS (Fig. 5f,g). However, MDA-MB-231 did not show significant changes in either the two measurements. This could be explained by their aggressive phenotype, which are triple negative breast cancer (TNBC), leading to more reliance on OXPHOS metabolism which was shown to have relatively higher OCR in comparison with MCF7 (Fig. 5f). This finding also suggests that the Warburg effect does not consequently mean that cancer cells fully rely on glycolysis as energy metabolism, but still maintain OXPHOS metabolism and is activated accordingly to cancer phenotypes. FIBIS also points out relatively higher bound fraction NADH in MDA-MB-231 than in MCF7 which verifies our finding using two completely different approaches.

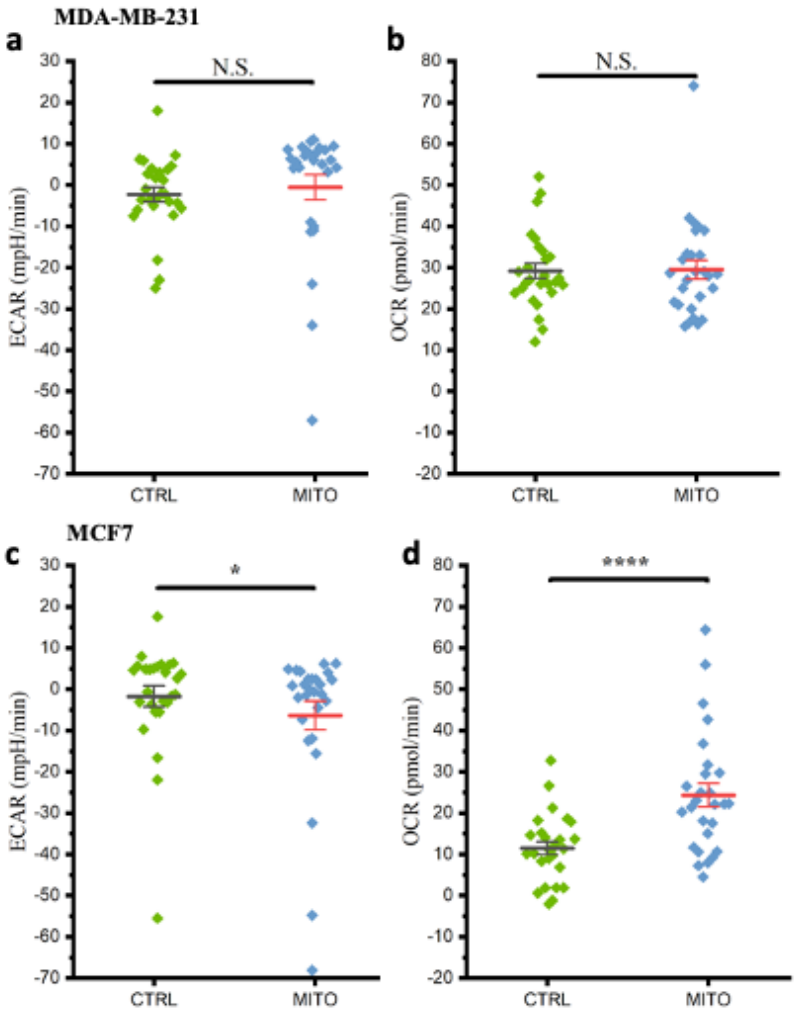

Figure 3. 8 Seahorse XF analyzer. Extracellular acidification rate (ECAR) represents glycolysis where oxygen consumption rate (OCR) represents OXPHOS. a,b) MDA-MB-231 did not show any significant change in both parameters. c,d) Respiration of MCF7 significantly increased after consuming epithelial mitochondria and a decrease in ECAR. p-values are calculated using two-tail paired Student's t-test. N = 45. * indicates $p < 0.05$ and **** indicates $p < 0.00001$. Data are represented as mean ± S.D. ranges.

3.4.5 Mitochondrial membrane potential analysis

To confirm the continued activity of transferred mitochondria upon entering host cells, we utilized Tetramethylrhodamine methyl ester (TMRM), a cell-permeable, cationic dye frequently employed to measure mitochondrial membrane potential in live cells, to analyze mitochondrial intensity changes. The magnitude of membrane potential directly relates to

electron transport efficiency and ATP production, allowing us to infer mitochondrial activity levels[17,56]. Higher membrane potentials correspond to increased active mitochondria and more efficient energy production, whereas lower potentials indicate a decline in mitochondrial activity and energy production. By targeting previously labeled mitochondria in host cells, we measured fluorescence intensity within the 570-590nm wavelength range. Our findings demonstrated that transferred mitochondria remained active after entering BCCs (as depicted in the figure). Additionally, TMRM intensity levels significantly increased in MCF7s after mitochondria transfer (Fig. 2c), implying the enhancement of proton pumps in Complexes I and III, which are crucial components during oxidative phosphorylation (OXPHOS). The rise in TMRM intensity solely in MCF7s, but not in MDA-MB-231s, correlated with Seahorse XF analyzer results, indicating metabolic shifts in MCF while MDA-MB-231 sustained a high respiration rate.

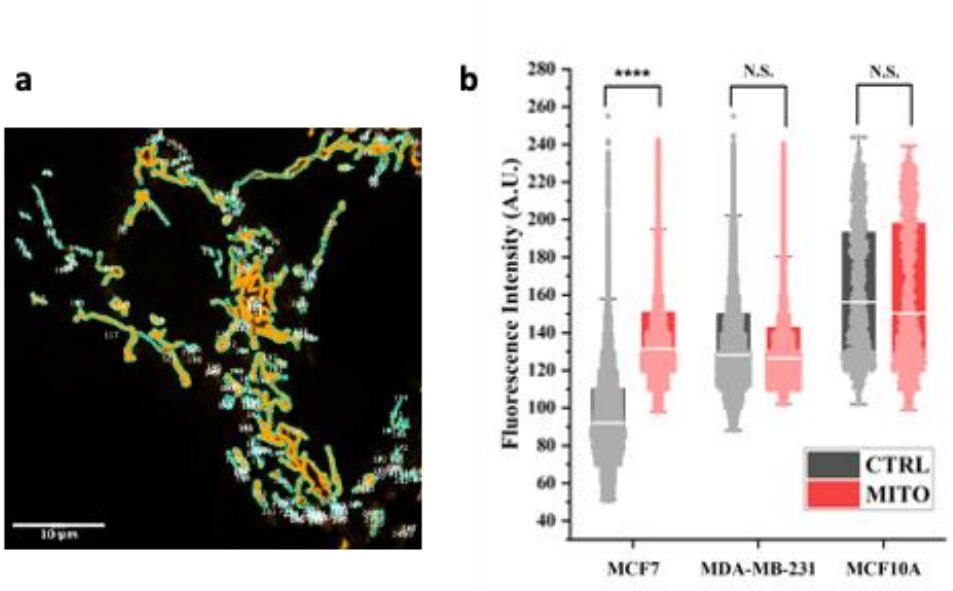

Figure 3. 9 TMRM membrane potential analysis. a) Automatic Otsu threshold masking of TMRM labeled mitochondria in MCF7 with transferred mitochondria segmented by imageJ. b) Significant increase was found in MCF7 Mito group indicating enhanced mitochondrial activity. N = 9211, 7907, 4185, 5670, 5350, and 6124 for MCF7 control, mitochondria, MDA-MB-231 control, mitochondria, MCF10A control, and mitochondria respectively. Data are represented as mean ± interquartile ranges. p-values are calculated using two sample Kolmogorov-Smirnov test. N.S. indicates none significance and **** indicates $p < 0.00001$.

3.5 Discussion

In this chapter, we have presented several metabolic assays to elucidate the impact of transferred mitochondria on BCCs. Our findings from the Seahorse assay and TMRM analysis suggest that MCF7s enhanced their respiration rate, leading to an increase in ATP production, while MDA-MB-231s maintained a high oxidative phosphorylation (OXPHOS) metabolic state, a hallmark of triple-negative cancer cells. Nevertheless, FIBIS results indicate that MDA-MB-231s were also affected by transferred mitochondria, as evidenced by an increased fraction of bound NADH, indicating an enhancement of respiration beyond their initial state. This effect was corroborated by the cell viability assay results presented in Chapter 2, where the

proliferation rate of MDA-MB-231s was more significant than that of MCF7s when treated with transferred mitochondria. Combining the TMRM analysis of individual mitochondria with the gold standard Seahorse assay results, we have demonstrated that FIBIS is a suitable and more sensitive method to quantify the metabolic state and dynamics of single mitochondria.

CHAPTER 4. DETECTION AND QUANTIFYING OF REACTIVE OXYGEN SPECIES

4.1 Abstract

Reactive oxygen species (ROS) play a complex role in cancer development and progression[17]. While ROS are natural byproducts of cellular metabolism and are involved in normal physiological processes, excessive ROS production can result in oxidative stress, causing DNA damage, genomic instability, and cellular dysfunction. However, cancer cells often exhibit elevated antioxidant defenses to counteract ROS, allowing them to survive and proliferate under oxidative stress conditions. Understanding the delicate balance between ROS and antioxidant defenses in cancer cells is crucial for developing targeted therapies that exploit their vulnerability to oxidative stress while sparing normal cells. This chapter investigates the influence of stimulated ROS from secondary organic aerosols (SOA), a major fraction of fine particulate matter, towards normal macrophage cells. Through our cellular imaging techniques including the phasor approach to FLIM and third harmonic generation imaging, we show that PQN and isoprene SOA activate NADPH oxidase in macrophages to release massive amounts of superoxide in a time dependent manner and inflate the cell membrane structure. While higher exposures trigger cellular antioxidant response elements, the released ROS induce oxidative damage to the cell membrane through lipid peroxidation. Such quantitative understandings provide a basis for further elucidation of oxidative stress level in cancer cells.

4.2 Introduction

ROS are chemically reactive molecules that include free radicals[57–59], such as superoxide anion (O_2·-), hydroxyl radical (·OH), and non-radical species like hydrogen peroxide (H_2O_2). ROS are generated as natural byproducts of normal cellular metabolism, primarily in the mitochondria, peroxisomes, and cytoplasm. They serve as important signaling molecules involved in various cellular processes, including cell proliferation, differentiation, and apoptosis.

While ROS play essential roles in cellular signaling and defense against pathogens, their levels must be tightly regulated within cells. When ROS production exceeds the capacity of cellular antioxidant systems to neutralize them [60–62], a state of oxidative stress occurs. Oxidative stress arises from an imbalance between ROS production and the cell's antioxidant defenses, leading to an excessive accumulation of ROS. Excessive ROS levels can have detrimental effects on cells. ROS can react with and damage various cellular components, including lipids, proteins, and DNA. Such oxidative damage can disrupt cellular function, impair DNA integrity, and contribute to genomic instability. Accumulated DNA damage caused by ROS can lead to mutations and increase the risk of cancer development. Hence, it is essential for understanding oxidative stress-related processes and their impact on cellular health.

To address the aforementioned requirements, this chapter explores the mechanism of stimulated reactive oxygen species (ROS) production in macrophages when exposed to secondary organic aerosols (SOAs). SOAs constitute a significant fraction of particulate matter (PM) and are formed through the atmospheric oxidation of volatile organic compounds (VOCs)[63–65], resulting in the generation of various oxygenated compounds, including hydroperoxides and alcohols. Upon inhalation and deposition of PM in the respiratory tract's epithelial lining fluid[66,67], these compounds come into contact with macrophages, which are the initial cellular responders of the innate immune system responsible for safeguarding the lungs against infections caused by bacteria, microbes, and pathogens. This defense mechanism involves the release of ·O2− through phagocytosis, a process referred to as the "respiratory burst"[68–70], which transiently consumes oxygen. By employing the phasor approach to fluorescence lifetime imaging microscopy (FLIM), we demonstrate a time-sensitive positive correlation between the respiratory burst's superoxide production and the activation of NADPH oxidase. Notably, the phasor distribution revealed a prolonged lifetime component following the peak of superoxide production, indicating the occurrence of lipid peroxidation. Additionally, we employed Laurdan fluorescence lifetime imaging and third-harmonic generation (THG) microscopy to examine the impact of PQN and isoprene SOAs on cell membrane fluidity and lipids, respectively. These cellular imaging techniques provide spatial information on NADPH oxidase activity within live cells and enable quantification of the damage inflicted by

accumulated ROS levels. Our study represents the first attempt to analyze the free and bound fractions of NAD(P)H over a time course, serving as a means to monitor NADPH oxidase activity, with findings supported by results obtained from our collaborators in the Chemistry department using Electron Paramagnetic Resonance (EPR) Spectroscopy.

4.3 Material and Methods

4.3.1 Cell culture and Cytotoxity

Macrophage cells (ATCC® TIB-71™) were obtained and passaged in complete media (DMEM media supplemented with 10% FBS and 1% penicillin streptomycin) until >80% confluent. Cells were then seeded at a density of 4×10^4 cells/mL with 200 µL per well into 96-well plates (Corning) and incubated at 37 °C and 5 % CO_2 in an incubator for about two hours for cells to fully adhere to the bottom of the culture plate. Cell density was kept the same for superoxide measurements and cell imaging.

4.3.2 NAD(P)H Phasor Approach to FLIM

The NADPH oxidase complex[71] is an important source of $\cdot O_2^-$ in phagocytosis as activated by bacterial products and cytokines. The activation of NADPH oxidase generates $\cdot O_2^-$ through the reaction: $NADPH + 2O_2 \rightarrow NADP^+ + H^+ + 2\cdot O_2^-$ Here we utilize the auto-fluorescence of NADPH measured with FLIM combined with experiments using NADPH oxidase activator

PMA[72] and inhibitor Apocynin to study the NADPH oxidase activities. It should be noted that NADH (nicotinamide adenine dinucleotide) has identical fluorescence properties with NADPH[73], thus FLIM cannot differentiate NADH and NADPH and we denote the FLIM signals as NAD(P)H. Note that NADH reacts with oxygen to produce either water or H_2O_2, or produces significantly lower $\cdot O_2^-$ than NADPH. NAD(P)H expresses in two forms inside cells, bound and free states. Different Therefore, the relative locations on the trajectory can be used to obtain the bound NAD(P)H fractions and the decrease of bound NAD(P)H fractions indicates the activation of NADPH oxidase activities.

For FLIM imaging, cells were seeded at a density of 4×10^4 cells mL^{-1} and incubated overnight before exposure to PQN and isoprene SOA for imaging. PQN and SOA in media in the absence of cells produced low fluorescence background signals. Cells were imaged at 37 ℃ and 5% CO_2 environment before exposure and at different time points after the addition of samples. Since NAD(P)H mainly reside in cell membranes and cytoplasm [62] and that the fluorescence lifetimes of nucleus do not change significantly before and after sample exposure, nucleus were cropped out, i.e., only the fluorescence signals from the cell membranes and cytoplasm were included in calculating the bound NAD(P)H fractions. The bound NAD(P)H fractions from all data points for each sample were averaged from multiple cells (N = 12-23) and shown on Fig. 4.2. PQN exhibited an unusually long fluorescence lifetime distribution and the phasors from PQN fall outside of NAD(P)H free-bound trajectory. We conducted hyperspectral imaging to

confirm that the long fluorescence lifetime was caused by phosphorescence from triplets of PQN[74]. To avoid the lifetime of phosphorescence interfering with the NAD(P)H fluorescence lifetime, we used PBS buffer to wash cells after 10 minutes of incubation. After replacing with fresh incomplete media, cells were loaded back to the FLIM system for imaging. With this method, the lifetime phasors of PQN fall onto the NAD(P)H free-bound trajectory as shown in Fig. 4.2.

4.3.3 Laurdan Probe Lifetime Analysis

The FLIM-Laurdan imaging technique was employed to assess changes in cell membrane fluidity following sample exposure. To investigate membrane fluidity, a fluorescent membrane marker called Laurdan[75] (6-Dodecanoyl-2-Dimethylaminonaphthalene) was utilized. Laurdan is a solvatochromic probe known for its sensitivity to polarity, allowing it to insert into lipid bilayers at various depths and orientations. This enables the detection of hydrophobic environments by altering its spectral emission maximum. When located in a hydrophobic environment, Laurdan exhibits at least two excited states: the locally excited state, inherent to the fluorophore itself, and an internal charge transfer state induced by a larger dipole moment. This polar "relaxation" prompts water molecules in more hydrophilic environments to align with Laurdan's dipole orientation, resulting in energy loss. Consequently, a spectral red shift in its emission is observed. Furthermore, the fluorescence lifetime of Laurdan can be measured

and quantified to identify lipid-ordered and disordered phases[76]. A decrease in Laurdan fluorescence lifetime in the blue channel (460/80nm) indicates an increase in membrane fluidity caused by lipid peroxidation. To conduct the experiment, cells were seeded in an 8-well plate, and complete media was replaced with incomplete media. Subsequently, Laurdan dye was added to each well, achieving a final concentration of 5 μM. The cells were then incubated under their respective cellular conditions for 30 minutes before exposure to control, PQN, PMA, and isoprene SOA. After a specified exposure period, the cells (4×104 cells mL-1) were loaded into the FLIM system for imaging using an 800 nm excitation wavelength.

In terms of quantification, we image segmented only membrane parts of the macrophage FLIM images and used a **tau modulation** projecting all pixels onto the universal circle giving us absolute lifetime values (Fig. 4.1). This modulation was appropriate due to phasors of Laurdan lifetime in the blue channel are approximately aligned to the universal circle. Original phasor plots are formed within the universal semi-circle (equation 1.) given coordinates (G,S). Tau modulation uses a circle of radius ψ (equation 2.) to project pixel coordinates onto universal circle giving single exponential lifetime (equation 3.).

$$(G - 0.5)^2 + S^2 = 0.25$$

$$G^2 + S^2 = \psi^2$$

$$G_{proj} = \psi^2$$

$$\tau = \sqrt{(1 - G_{proj})/(G_{proj} * \omega^2)}$$

Where G_{proj} is the projected G coordinate, ω is the laser modulation frequency, and τ is the single exponential lifetime we acquire.

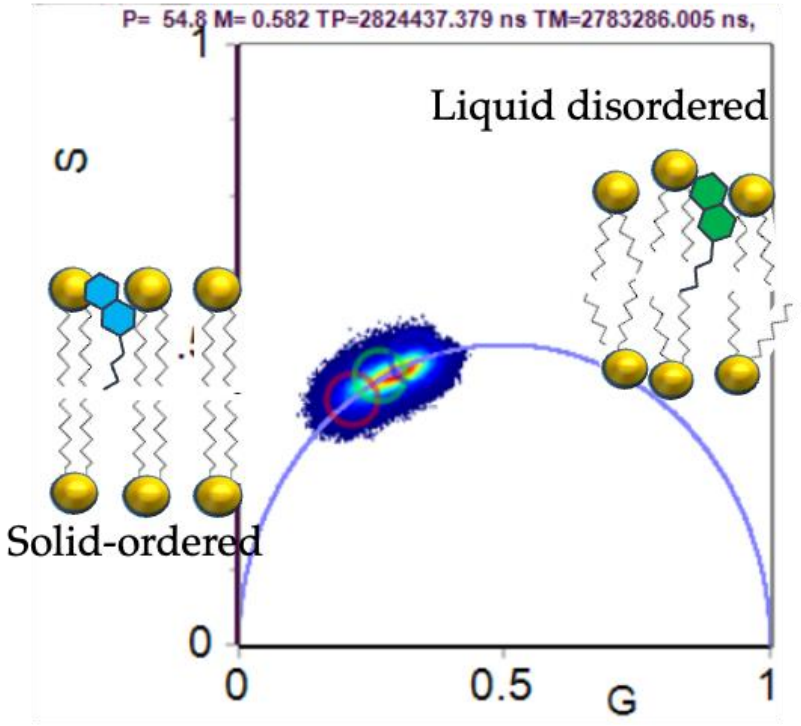

Figure 4. 1 Laurdan phasor plot. Laurdan in solid-ordered membrane has a relatively longer lifetime than liquid disordered membrane. The lifetime change follows mono-exponential decay and is simple to calculate using Tau modulation method.

4.3.4 Third Harmonic Generation (THG) Imaging

The THG imaging technique was applied to detect the accumulation of lipids inside the cells after exposure to isoprene SOA and PQN. The excitation of THG signal requires laser wavelengths of up to ~1000 nm, which conventional tunable Titanium Sapphire lasers could not achieve. The THG imaging was carried out in the Deep Imaging Via Emission Recovery (DIVER) system from the LFD[77], which uses Spectra Physics Insight DS+ femtosecond laser tunable in the range of 68 - 1300 nm. The actual focal depth difference was found to be ~0.75

mm for different wavelength excitation, where NAD(P)H is 740 nm and THG is 1050 nm. THG signal is generated at the interface between media with difference in third order nonlinear susceptibility, refractive index and dispersion, and can be used to detect lipids. The THG images were taken before and after 10-min exposure to isoprene SOA and PQN. Note that THG microscopy is not affected by long lifetime phosphorescence from PQN.

4.4 Results

4.4.1 Cellular Superoxide Release by NADPH Oxidase Activation

Cellular imaging techniques were employed to investigate the mechanism of cellular superoxide (·O2-) release. Specifically, we used selected doses known to induce substantial cellular ·O2- release. Phasor approach to FLIM analysis was performed to examine the distribution of cell membrane and cytoplasmic components along a metabolic trajectory represented by a line connecting the positions of free and bound NAD(P)H on a phasor plot (Fig. 4.2 a). This trajectory was utilized to determine the fractions of bound NAD(P)H. When macrophages were exposed to PQN and isoprene SOA, a decrease in the bound NAD(P)H fractions compared to controls was observed. This indicates oxidation of the bound state NADPH to non-fluorescent NADP+, resulting in the release of superoxide: NADPH + 2O2 → NADP+ + H+ + 2·O2-. In contrast, exposure to phorbol 12-myristate 13-acetate (PMA), a commonly used inducer to activate NADPH oxidase and increase endogenous ·O2- production,

led to a shift from the bound to free state of NAD(P)H. Moreover, the presence of apocynin (Apo), a specific NADPH oxidase inhibitor, increased the bound NAD(P)H fractions compared to cells without inhibitors. Notably, due to interference from phosphorescence of PQN, inhibitor experiments for PQN were not available. Considering the differences in doses and exposure times for FLIM imaging, direct comparison of the bound fractions in Fig. 4.2 b for PQN and isoprene SOA is not feasible. Furthermore, apocynin significantly reduced cellular ·O2- production upon exposure to PQN, isoprene SOA, and PMA (Fig. 4.2 c), strongly suggesting that PQN and isoprene SOA primarily trigger cellular ·O2- production by activating NADPH oxidase. Interestingly, when apocynin was present in controls, the bound NAD(P)H fraction was higher compared to isoprene SOA and PMA with apocynin. This could be attributed to an increase in NADH bound fractions resulting from enhanced mitochondrial oxidative phosphorylation (OXPHOS). Recent studies have shown that Apo can enhance ATP production and mitochondrial membrane potential, which are regulated by OXPHOS. This observation implies that exposure to PQN and isoprene SOA may induce a certain level of mitochondrial dysfunction, although dedicated studies are needed to further explore this aspect.

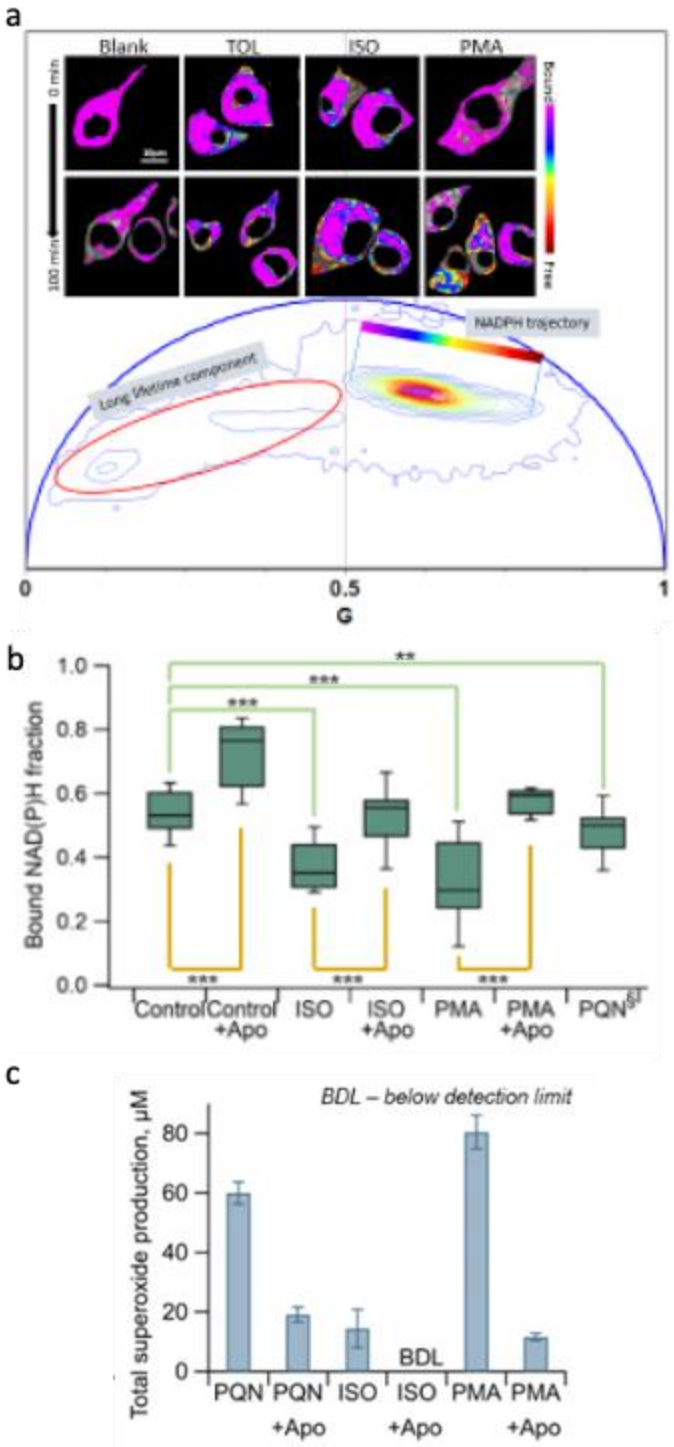

Figure 4. 2 NADPH oxidase activities. a) NAD(P)H phasor plot of macrophages exposed to TOL, ISO, and PMA for 100 minutes. Pseudo colored images show the bound fraction of NADPH starting from membrane part of the cell indicating the location of NADPH oxidase. Long lifetime component appeared 60 minutes after exposure which is when superoxide production rate stops. b) NAD(P)H bound fractions analysis for macrophages treated with the control and samples with and without NADPH oxidase inhibitor apocynin (Apo). (C) Effect of apocynin on total superoxide production. Bars with error bars represent the average from triplicates and the standard deviation. Unpaired t-test, ***$p < 0.0001$ and **$p < 0.001$. ISO and PMA denote isoprene SOA and phorbol 12- myristate 13-acetate, respectively.

4.4.2 Phosphorescence from PQN dominates fluorescence lifetime

The long lifetime component being discovered in Fig. 4.2 a was similar to lifetime features of oxidized lipids mentioned in Datta *et al* work[78] which stands a critical supporting point of lipid peroxidation. However, the dynamic change of phasor distribution for PQN was suspected to be caused by another contributing factor known as phosphorescence. Phosphorescence is also known to emit photons from excited electrons. Unlike fluorescence, which is immediate and short-lived, phosphorescent materials store and release energy gradually, resulting in a lifetime in milliseconds range. To validate the assumption of strongly contributed long lifetime components is caused by phosphorescence, we used lambda mode to collect the emission spectrum excited by 740nm two photon laser and found a strong intensity peak being accumulated <450nm (Fig. 4.3 b) which matches with phosphorescence spectrum of 9,10-phenanthrenequinones[79]. These pixels were also overlapped with the long lifetime phasors (Fig. 4.3 c) confirming the PQN phosphorescence location. Since phosphorescence interferes with fluorescence photon arrival times, we made an effort to wash out PQN using PBS and immediately image macrophages undergoing NADPH oxidase. Within 10 minutes, Fig. 4.3 d shows that PQN also follows the decreased fraction in bound state NAD(P)H, indicating release of superoxide.

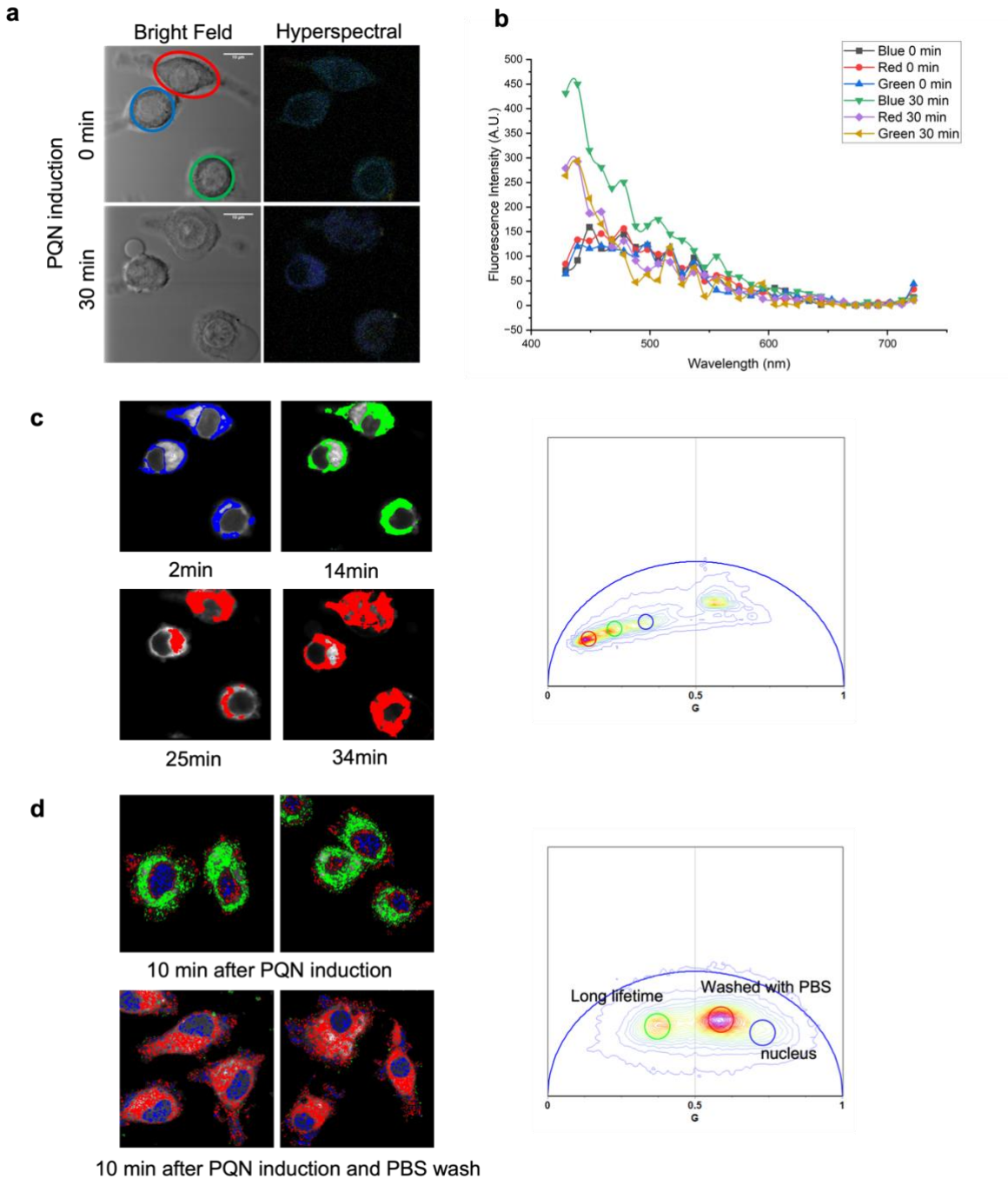

Figure 4. 3 Phosphorescence detection of PQN. a) Bright field images of macrophages before and after 30 minutes induced with PQN indicates the morphology change of cell membrane. b) Emission peak at 445nm wavelength was detected after 30 minutes of PQN induction. c) Colored cursors imply the increased lifetime accordingly to incubation time. d) Macrophages washed with PBS avoids phosphorescence interference in image pixels and regains fluorescence lifetime information of live cells.

4.4.3 Oxidative Stress on Cell Membranes

To assess the impact of PQN and isoprene SOA on cell membranes, we conducted measurements of lifetime changes using the solvatochromic probe Laurdan and Third Harmonic Generation (THG) imaging after exposure. The FLIM-Laurdan images can be seen in Fig. 4.4 c. As Laurdan dye is specifically incorporated into the hydrophobic regions of the membrane, only fluorescence signals originating from the cell membranes were selected for calculating the fluorescence lifetime. A total of 15 cells were averaged for each sample, and the results were presented as violin plots in Fig. 4.4 d. We observed significant decreases in the fluorescence lifetimes of Laurdan on cell membranes of macrophages exposed to PQN, isoprene SOA, and PMA. This indicates that these samples induce an increase in membrane fluidity, an important parameter related to membrane integrity and cell health. Additionally, THG microscopy imaging revealed an increase in THG signal surrounding the cell membranes upon exposure to PQN and isoprene SOA, suggesting lipid accumulation (Fig. 4.4 a). Bright-field cell images also suggested the formation of foam cells, where macrophages may have taken up oxidized low-density lipoprotein (LDL). This process is known to involve the activation of NADPH oxidase, as observed in previous studies. Considering that the doses of PQN and isoprene SOA used were 1.74 μg mL-1 and 305 μg mL-1, respectively, and cellular ·O2- production dominates over chemical production, it is likely that macrophages undergo lipid peroxidation caused by ·O2- or other reactive oxygen species (ROS) generated

subsequently. The violin plots provided insight into the decrease in Laurdan lifetime induced by SOA molecules. PQN, which produces the highest amount of superoxide, resulted in the most severe damage to the cell membrane. The broader tails of the violin plots with even shorter lifetimes suggest that internal membranes are also affected by PQN. Furthermore, we observed that the magnitude of lifetime decrease is dependent on the concentration of the induced SOA molecule. In the case of macrophages treated with isoprene SOA and the addition of manganese superoxide dismutase (Mn-SOD), the Laurdan lifetime was relatively higher compared to treatment with isoprene SOA alone. This raises the question of whether SODs are capable of protecting cell membranes from free radical attacks. In conclusion, the use of tau modulation violin plots can serve as a quantitative method to assess the healthiness of cell membranes.

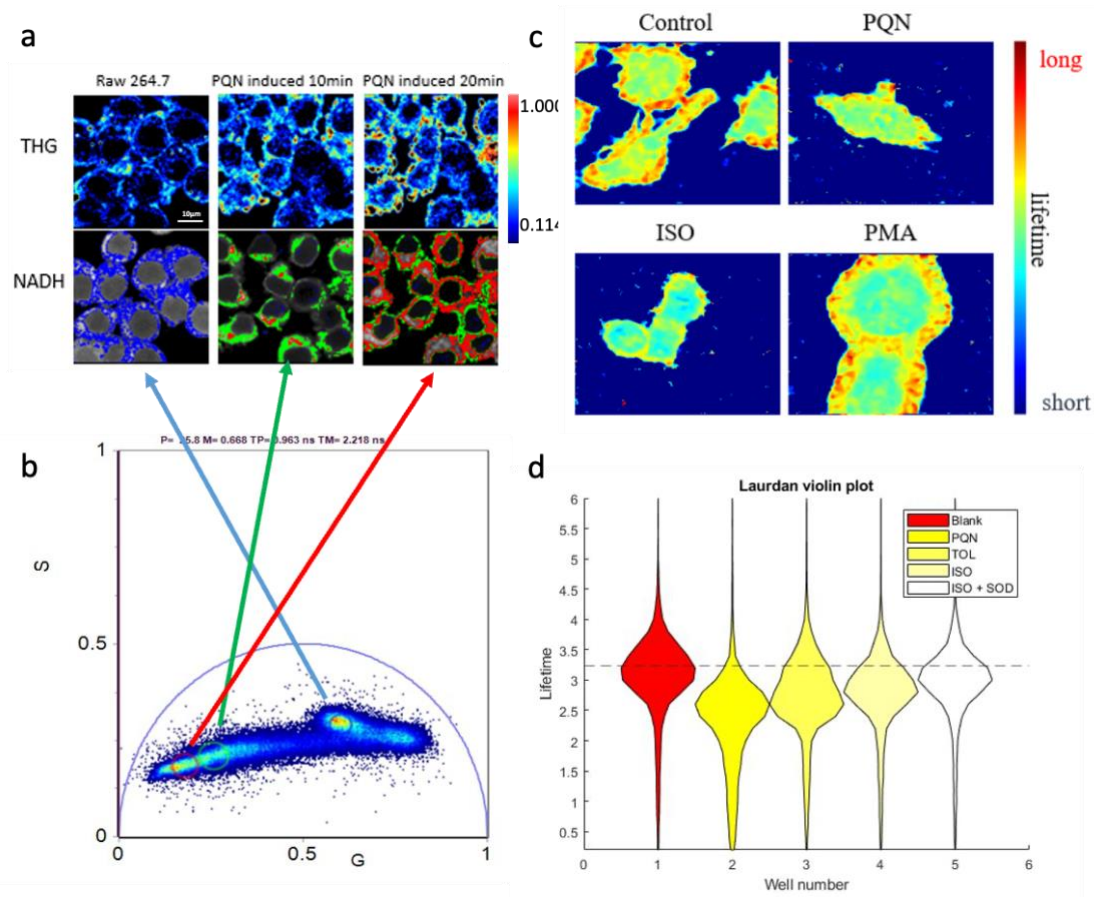

Figure 4. 4 Quantification of cell membrane damage. a) THG signal images present increasing lipid droplets in the upper panel and in the bottom panel shows cursor derived images referenced from b) phasor plot collected from the DIVER system. c) Laurdan lifetime analysis of macrophage cell membranes. PQN and ISO shows decrease of lifetime at the cell membrane indicating hydrophobic environment for the macrophages.

4.4.4 Time dependent superoxide production rate

Diogenes chemiluminescence assay was measured every 3 minutes for a total of 4 hours observation time. The superoxide production rate was found to peak at 45 minutes and 50 minutes post inducement of ISO and PMA. Comparing the results from both chemical and fluorescence lifetime approaches, the production rate of superoxide is observed to follow a time dependent pattern suggesting the final stage of ROS production and entering oxidized lipid

phase. The phasor approach to NAD(P)H FLIM was capable of reflecting subtle changes of free to bound fraction NADPH within 10 minutes of data collection time interval.

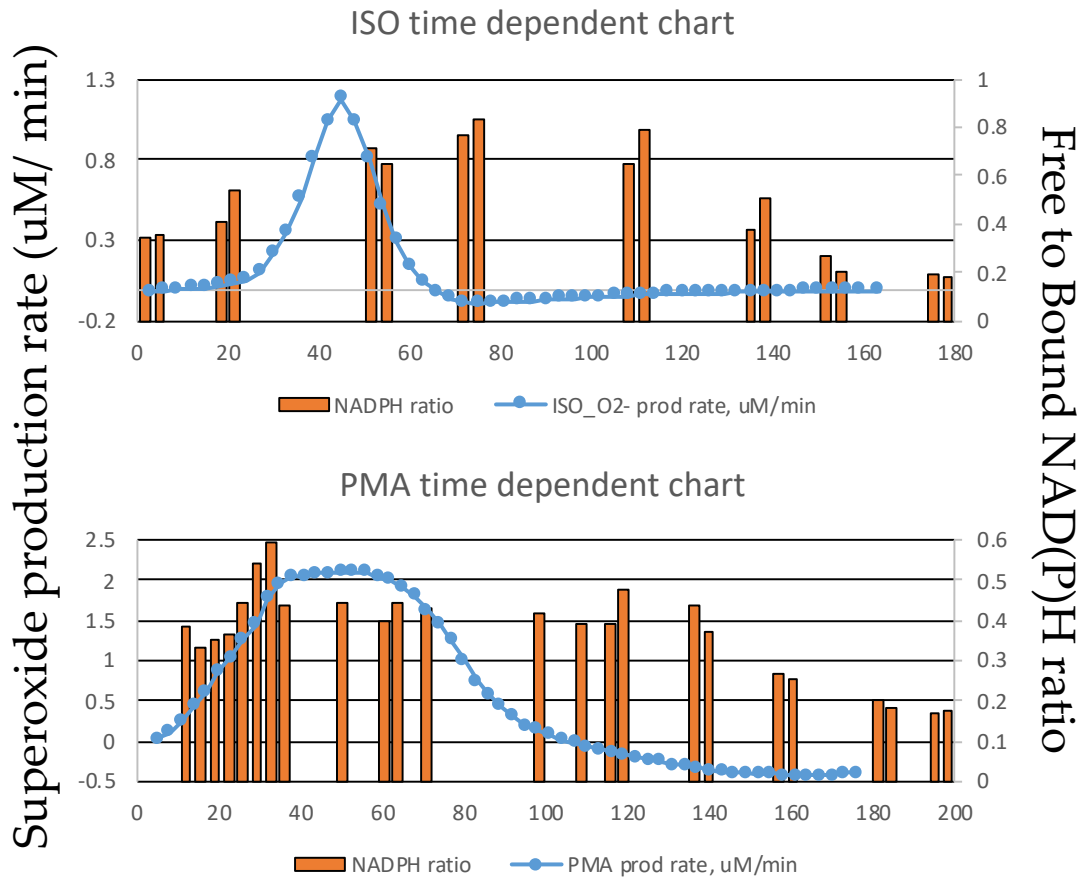

Figure 4. 5 Time dependent curve of free and bound fraction NAD(P)H.

4.5 Discussion

In macrophages, exposure to SOAs activates NADPH oxidase, which serves as a defense mechanism against xenobiotic particles. However, the macrophages fail to produce an adequate number of antioxidants to effectively reduce intracellular ROS levels, particularly superoxide. As a result, free radicals are able to attack cellular structures. Our objective was to assess the extent of ROS-induced damage to the cell membrane, as the presence of bubble foam

components in that region was observed. Analysis of THG images revealed an increase in lipid formation in the cell membrane, indicating degradation of the bilipid layer and compromising the barrier's integrity. Laurdan lifetime analysis demonstrated a reduction in lifetime after the induction of SOAs, indicating disorder within the bilipid layer. NAD(P)H lifetime provided information on NADPH oxidase activity and oxidative stress, as longer lifetimes were associated with these species. Initially, the presence of PQN super long lifetime interfered with the analysis, but we improved our methodology by washing out PQN phosphorescence with PBS, resulting in the same phasor distribution as ISO and PMA. Future directions include the use of Coherent anti-Stokes Raman spectroscopy (CARS) to verify oxidized lipids exists inside macrophage membranes. In conclusion, this chapter emphasizes the significance of intracellular ROS levels and their visualization and quantification in non-reversible lipid peroxidation and subsequent DNA damage caused by oxidative stress.

CHAPTER 5: LIGHTSHEET MICROSCOPY FOR MOLECULAR DYNAMICS IN 3D

5.1 Abstract

Fluorescence correlation spectroscopy (FCS) is a highly adaptable technique extensively employed for quantifying rates of chemical reactions, protein binding, interactions between nanoparticles and proteins, as well as biomolecular dynamics in both controlled laboratory settings (in vitro) and living organisms (in vivo). FCS is inherently suited for micro-scale investigations and can be effectively utilized in high-throughput screening for drug development. However, its applicability is often restricted to nanomolar concentrations, limiting its potential applications. In this study, we demonstrate how the utilization of massively parallel camera-based detection with side illumination significantly expands the usable concentration range of FCS by more than 100 times, enabling the measurement of low affinity processes. Our proposed approach, known as line-mean square displacement (line-MSD), is both robust and efficient, with acquisition times as short as 1 second, while eliminating the need for reference measurements to determine the size of the observed volume.

5.2 Introduction

By examining fluctuations in fluorescence caused by the movement of molecules within a minuscule observation volume (approximately 1 femtoliter), fluorescence correlation

spectroscopy (FCS) enables the measurement of diffusion and reaction kinetics, hydrodynamic radius, and particle concentration at the microscopic level[80]. Consequently, FCS has proven to be an exceptionally versatile tool extensively utilized for studying chemical reaction rates, protein binding, interactions between nanoparticles and proteins, as well as biomolecular dynamics in controlled laboratory settings (in vitro) and living organisms (in vivo)[81].Due to its inherently microscopic nature, FCS requires minimal sample volumes, rendering it particularly suitable for high-throughput screening applications, such as in drug design[82].While FCS exhibits remarkable sensitivity at low concentrations (picomolar to nanomolar), its application has historically been limited to the nanomolar concentration range, which somewhat restricts its potential uses. Recently, advancements in nanofabrication, super-resolution microscopy, and near-field probing techniques have expanded the usable concentration range of FCS[83–86]. However, the specialized hardware required for these methods hinders their widespread adoption. The side-SPIM, originally developed by Dr. Per Niklas Hedde as a light sheet microscope, offers additional degrees of freedom for sample manipulation within the system. Its perpendicular illumination of the light sheet compensates for noise sources that typically impede the application of FCS at high concentrations when using commonly used single point detectors. We demonstrate that our easily implementable approach extends the usable concentration range of FCS by over 100 times. This allows for the investigation of binding

processes in the micromolar concentration range, which can be crucial, particularly in drug design.

At high concentrations, FCS is commonly limited by noise, as the reduced amplitude of molecular fluctuations becomes insignificant compared to other sources of fluorescence signal variation, such as laser and detector noise. However, as long as the measured molecular brightness (i.e., the number of photons detected per molecule per time interval) remains constant, the signal-to-noise ratio of an FCS measurement theoretically remains independent of the concentration[87]. However, in practice, highly sensitive single point detectors like photomultipliers (PMTs) and avalanche photodiodes (APDs) have a limited count rate at high fluorophore concentrations, necessitating a reduction in excitation intensity to avoid detector saturation. This reduction in excitation intensity subsequently diminishes the number of fluorescence photons emitted per molecule per time interval. Consequently, this limitation in the measured molecular brightness decreases the sensitivity of FCS at high concentrations.

Nanofabrication, super-resolution, and near-field techniques overcome this issue by further reducing the observation volume to the femtoliter scale, ensuring that the average number of observed molecules remains low even at higher concentrations. However, these approaches require specialized nanosized sample containers, specific fluorophores, and/or powerful yet expensive pulsed lasers, with only a moderate expansion of the usable concentration range. Others have mitigated laser noise by compensating with data from a photodiode monitoring

the laser output power and extended the detector saturation limit by splitting the fluorescence signal across multiple APDs[88], which necessitates substantial technical efforts.

In contrast, we capitalized on the abundant pixel count available in modern sCMOS cameras for parallelized detection across more than 16 lines, each consisting of over 240 pixels, recorded at a rate exceeding 10,000 Hz. This massively parallel detection enabled us to handle an exceptionally high photon flux while simultaneously compensating for non-molecular signal fluctuations using spatial averaging within the lines. To create an axially confined observation volume, we employed a thin beam (~1-2 μm diameter) for side illumination of the sample, which was subsequently imaged onto an sCMOS camera, resembling the geometries utilized in light sheet microscopy [89]. Through this line illumination (LIM) approach, we accurately determined the diffusion coefficient of a small dye molecule (Atto 488) in aqueous solution at concentrations up to 30 μM. In an initial application, we characterized the low-affinity binding of fluorescein isothiocyanate (FITC) to bovine serum albumin (BSA). Lastly, we demonstrate how the LIM method can be employed to track the motion of fluorescently labeled biomolecules within live cells.

5.3 Material and Methods

5.3.1 Line Illumination

Our setup was based on the sideSPIM as previously described[89]. The output of a 488-nm laser (Omicron-Laserage, Rodgau-Dudenhofen, Germany) was spatially cleaned with a single mode fiber, reflected on a 2-axis galvo mirror system (Cambridge Technology, Bedford, MA, USA), and passed through a scanning lens (f = 50 mm) and tube lens (f = 180 mm) in a 4f configuration. A 4×, NA 0.16 objective lens (Olympus, Center Valley, PA, USA) was used the generate a Gaussian illumination beam with a waist size of 1.9 μm and a confocal parameter of 48 μm inside our custom sample chamber. Sample fluorescence was collected with a 60×, NA 1.0 water immersion lens (Olympus), separated from scattered excitation light with a 535/40 nm bandpass filter (Chroma, Bellows Falls, VT, USA), and focused via the internal tube lens of an inverted microscope body (IX71, Olympus) onto the chip of a sCMOS camera (PCO, Kelheim, Germany). The pixel size at the sample was 108 nm.

5.3.2 Single Point FCS

Single point FCS was measured using Zeiss LSM880 equipped with the FCS module (Carl Zeiss, Jena, Germany). Sample fluorescence was excited with a 488-nm Argon laser line reflected off the internal dichroic (MBS488) and passed through a 40×, NA 1.2 water immersion objective (Zeiss). Fluorescence was focused onto a pinhole of 35 μm diameter (1

Airy unit) before detection within a range of 500 nm–600 nm. To calibrate the size of the point spread function, a 10 nM solution of Rhodamine 110 was prepared in PBS buffer and the beam waist of the resulting data was fitted by fixing the diffusion coefficient at 440 μm2/s [90]. For fitting of the correlation function, G(τ), as a function of the lag time, τ, we used a free diffusion model

$$G_{(\tau)} = \frac{\gamma}{N}\frac{1}{1+\frac{4D\tau}{\omega^2}}\frac{1}{\sqrt{1+\frac{4D\tau}{S\omega^2}}}$$

with N the resulting average number of particles inside the observation volume, γ = 0.35 the correction factor for the Gaussian shape of the point spread function, S = 5 the aspect ratio (latera to axial extension), ω = 0.20 μm the lateral beam waist, and D the resulting diffusion coefficient, which is related to the diffusion time τD = ω^2/4D.

5.3.3 Dye and Protein Solutions

Atto 488 (#41051-1MG-F, Sigma-Aldrich, St. Louis, MO, USA) was dissolved in PBS buffer to a stock concentration of 100 μM, determined by measuring the absorption at 490 nm (Nanodrop, ThermoFisher, Waltham, MA, USA). Serial dilutions in PBS buffer of 30, 100, and 300 nM, as well as 1, 3, 10, 30 and 50 μM were placed in our custom imaging chamber. FITC (#1245460250, Sigma-Aldrich) and BSA (#A7906-10G, Sigma-Aldrich) were diluted in PBS buffer to generate stock solutions of 74 μM and 3 mM, as determined by absorption

measurements at 490 nm and 280 nm, respectively. For both solutions, the pH was adjusted to 9 by adding 5 N NaOH to increase the fluorescence quantum yield of FITC.

5.3.4 Cell Sample Preparation

MCF10A (American Type Culture Collection, Manassas, VA, USA) cells were cultured in DMEM/F12 with high glucose, sodium pyruvate, and L-glutamine (Thermo Fisher Scientific, Waltham, MA, USA) supplemented with 5% horse serum (Thermo Fisher Sci- entific), 20 ng/mL epidermal growth factor, 0.5 mg/mL Hydrocortisone (Sigma-Aldrich), 100 ng/mL cholera toxin (Sigma-Aldrich), 10 μg/mL insulin (Sigma-Aldrich), and 1% Penicillin-Streptomycin 100× solution (Genesee Scientific, San Diego, CA, USA). Cells were plated in 35 mm dishes and transfected with plasmid encoding Arc-EGFP using Lipofectamine 3000 according to the manufacturer's protocol (Thermo Fisher Scientific). Collagen type I (Corning, Corning, NY, USA) gels were prepared at 2 mg/mL concentration by dilution with cell culture medium at 7.2 pH followed by polymerization inside sideSPIM imaging chambers[89] for 1 h at 37 ◦C. Cells were subsequently transferred to collagen type I gels and incubated for 12 h before imaging to allow for cell attachment to the gel. To visualize the cell nuclei, DNA staining with NucBlue (#R37605, ThermoFisher) was performed 15 min before imaging.

5.3.5 Measurement Parameters

Single point FCS data were measured at 1.7 mW laser power with 10 s acquisition times. For line-MSD analysis of Atto 488 and FITC binding to BSA, the laser output at the objective lens was set to 6 mW and 16 lines of 260 pixels were acquired at 10,246 Hz. A total of 100,000 frames were imaged for each data set (10 s acquisition time). For LIM analysis of Arc-EGFP in MCF10A cells, the laser power was reduced to 0.2 mW to prevent photobleaching. Due to the slower diffusion of Arc-EGFP in cells compared to the diffusion of free dye in aqueous solution, the camera exposure time was increased to 2 ms (500 Hz) and a total of 5000 frames were acquired for each cell.

5.3.6 Data Analysis

Each data set, I(x, y, t), was reordered, I(x, t, y), with ImageJ 1.53c and loaded into Matlab R2019a (Mathworks, Natick, MA, USA) for analysis, with 100,000 frames (t) of 16 lines (y) with 260 pixels (x). For each line, the spatial averages, $\langle I(x, t, y)\rangle_x$, and the spatio- temporal averages, $\langle I(x, t, y)\rangle_{x,t}$, were calculated and used to compensate for intensity fluctuations not attributed to molecule movement, such as laser fluctuations. The spatial averages represent the average intensity of all pixels in each line at any given time point and are therefore an intrinsic measure of the laser power. By dividing by the spatial averages and multiplying with

the spatio-temporal averages, i.e., the time average of the average intensity of all pixels in each line, the data can be normalized for the laser power:

$$J(x,t,y) = \frac{I(x,t,y)}{\langle I(x,t,y)\rangle_x}.\langle I(x,t,y)\rangle_{x,t}$$

Next, the immobile fraction (if present) was removed by subtracting the temporal average in each line. To avoid negative values in the resulting data set, the global average was subsequently added:

$$F(x,t,y) = J(x,t,y) - \langle J(x,t,y)\rangle_t + \langle J(x,t,y)\rangle_{x,t,y}$$

For each line of the 16 lines × 260 pixels × 100,000 frame data set, Fy(x,t), these data were then space-time correlated:

$$G_y(\zeta,\tau) = \frac{\langle F_y(x,t).F_y(x+\xi,t+\tau)\rangle}{\langle F_y(x,t)\rangle^2} - 1$$

To the resulting correlation function, a Gaussian model,

$$H_\tau(\xi) = A \cdot \exp\left(-(\frac{G_\tau(\zeta)-\zeta_0}{\omega})^2\right) + B$$

was fitted for each lag time, τ, with amplitude, A, offset, B, and width, w. The square of the fitted width, w2, which corresponds to the particle mean square displacement, was then plotted as a function of the lag time and the slope was determined by linear regression. From the slope, the diffusion coefficient was calculated as previously described[91].

5.4 Results

5.4.1 Line-MSD Method Validation

By utilizing Gaussian beam illumination (Fig. 5.1 a), only specific lines of the camera chip become relevant for capturing fluorescence emitted from the thin, tubular observation volume. In this region of interest, the frame rate of the camera can be increased to over 10,000 Hz, resulting in a pixel dwell time of less than 100 μs. Each pixel within each line of the acquired space-time (x, t) dataset (Fig. 5.1 b) is then correlated with all other pixels within the same line, generating a correlation map in space and time lag (ξ, τ) (Fig 5.1 c). For each line, a Gaussian function is fitted to this correlation map (Fig. 5.1 d). By plotting the width of these fitted Gaussians as a function of time lag (Fig. 5.1 e), the mean square displacement of the molecules can be determined, similar to the principles of image mean square displacement (iMSD) analysis[91,92]. Importantly, only two parameters are required to quantify these data: the pixel size at the sample, determined by the effective magnification of the objective, and the time interval between frames, determined by the camera's frame rate. In contrast to single point FCS, there is no need to calibrate the size of the observation volume to obtain the absolute value of the diffusion coefficient.

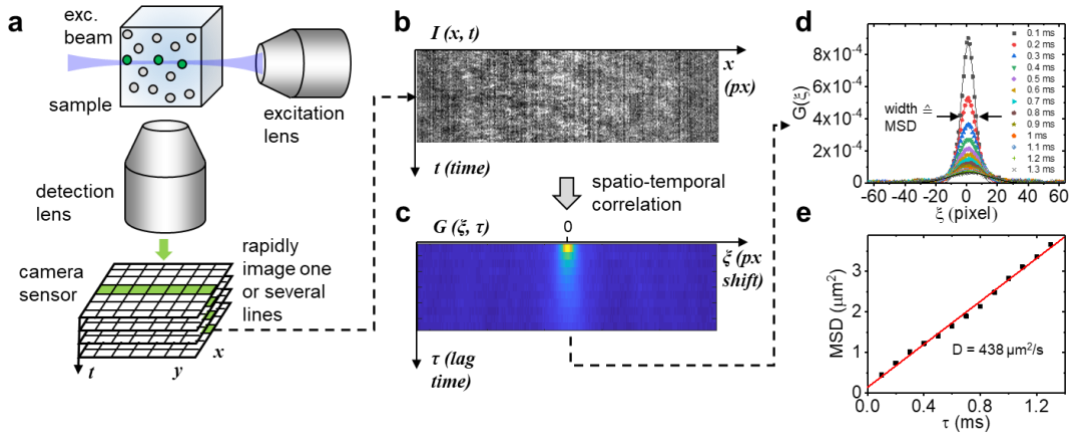

Figure 5. 1 Line excitation principle. a) A thin beam of light is injected into the sample from the excitation objective side and fluorescence is collected perpendicular to the beam direction with a high numerical aperture lens. A rapid time series of the resulting signal is collected with a fast camera. b,c) One or multiple lines are extracted from the this data set followed by spatiotemporal correlation of the space-time series. d,e) The correlation function for each lag time is fitted with a Gaussian distribution. The width of this distribution corresponds to the mean square displacement of the molecules under study and, plotted as a function of the lag time, the absolute diffusion coefficient can be determined from the slope.

To validate our approach, we began by measuring the diffusion coefficient of a small dye in an aqueous solution, the characteristics of which are well-known. We selected Atto 488 for this purpose due to its high water solubility, favorable photophysical parameters (quantum yield = 0.8, molar extinction coefficient = 90,000 in PBS at pH 7.4), and wide usage in fluorescence sensing applications. Atto 488, similar to many other small dyes with a molecular weight of around 0.8 kDa, exhibits a diffusion rate of approximately 400 µm²/s in aqueous solution at room temperature, necessitating a very high temporal resolution. We diluted the dye in PBS buffer at various concentrations ranging from 30 nM to 50 µM. For each concentration, we captured ten sets of 10,000 frames, with each set having a 1-second acquisition time. The measured diffusion coefficients are presented in Fig. 5.2 a. The insets in the figure depict photographs of the sample chamber filled with the Atto 488 solution, excited by 488-nm light.

At a dye concentration of 30 nM, the faint green fluorescence trace of the excitation beam/light sheet can be observed within the solution. The cyan background visible in the photograph arises from scattered 488-nm excitation light. Conversely, at a dye concentration of 50 µM, which represents a more than 1000-fold increase, all excitation light is completely absorbed, resulting in significantly stronger green fluorescence. Fig. 5.2 b illustrates three example concentrations measured using the line-MSD method, along with the corresponding single point FCS data fitted with a free diffusion model. Residuals are presented in Fig. 5.2 c and 5.2 d. It is worth noting that the low correlation amplitude observed in single point FCS at concentrations exceeding 100 nM led to overestimated diffusion coefficients.

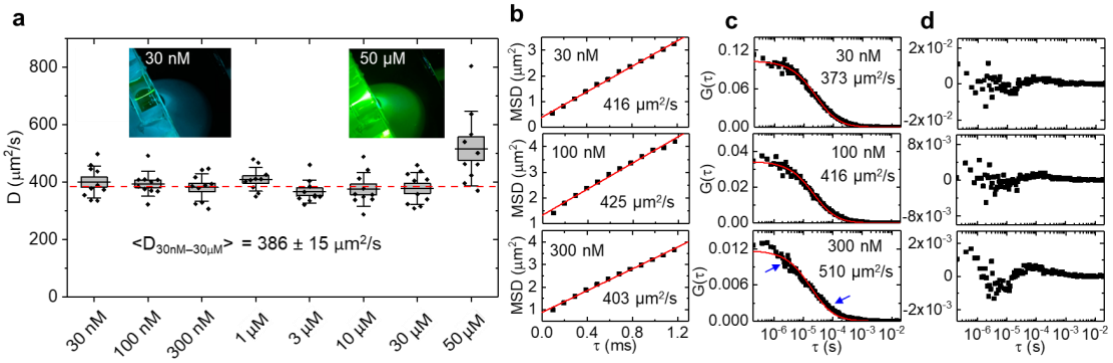

Figure 5. 2 Diffusion of Atto 488 in aqueous solution measured by Line-MSD. a) For each concentration, 10 measurements of 1 s duration were acquired; lines: averages, boxes: standard errors, whiskers: standard deviations. Dashed line: Average diffusion coefficient (386 ± 15 µm2/s, mean ± SD) of all measurements excluding 50 µM. Insets: Photographs of Atto 488 fluorescence at 30 nM and 50 µM. b) Example mean square displacement (MSD) of 1 s LIM data. c) Exemplary 10 s single point FCS data of the same solutions fitted with a free diffusion model and d) corresponding residual plots. At 300 nM, single point FCS overestimates the diffusion coefficient and deviates from the free diffusion model (see arrows).

5.4.2 Binding at High Concentration

Subsequently, we conducted a characterization of the weak binding interaction between fluorescein and bovine serum albumin (BSA)[93]. Fluorescein derivatives are widely employed for protein labeling purposes, while BSA, as the most abundant soluble protein in blood plasma, serves as a substitute for human serum albumin (HSA) in biological studies. BSA exhibits binding interactions with various biomolecules, including amino acids, fatty acids, and numerous small molecules, including drugs. Crystallography studies have identified three structurally similar binding domains (I, II, and III) within BSA[94]. To explore the interaction between fluorescein and BSA at high concentrations, we prepared serial dilutions of BSA ranging from 0.10 μM to 1 mM, each containing 4 μM of fluorescein. The resulting diffusion coefficients were measured using the LIM method at room temperature, as depicted in Fig. 5.3. Across the tested concentration range, a decrease in the diffusion coefficient of fluorescein was observed, reducing from 437 μm²/s (no BSA) to 135 μm²/s (1 mM BSA). Fitting the data to a simple binding model yielded a KD (dissociation constant) value of 178 ± 93 μM (mean ± SD). From the binding curve, the diffusion coefficient of the fluorescein-BSA complexes (with a molecular weight of 67 kDa) was estimated to be 68 μm²/s. This represents a 6.4-fold reduction in diffusion compared to free fluorescein (0.33 kDa), which is a highly reasonable result. As a point of reference, enhanced green fluorescence protein (EGFP), with 40% of the molecular weight (or 74% of the hydrodynamic radius) of BSA, was found to diffuse at approximately

90 μm²/s[91]. In principle, for fluorescein-BSA complexes, one would expect a ~5.9-fold reduction for a BSA monomer-fluorescein complex and approximately a 7.4-fold reduction for a BSA dimer-fluorescein complex relative to free fluorescein. Considering the millimolar concentration of BSA required for complete binding, it is expected that most complexes would consist of BSA dimers, as the monomer-dimer equilibrium of BSA has been measured with a dissociation constant of 10 ± 2 μM at 25°C[95].

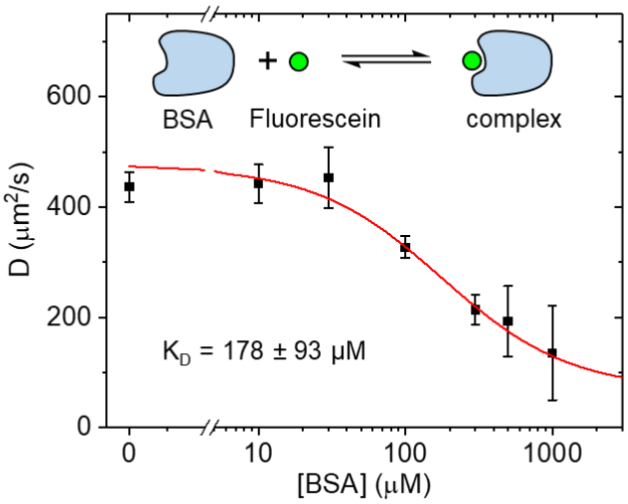

Figure 5. 3 Diffusion coefficients of fluorescein mixed with BSA at different concentrations. When bound to BSA, the diffusion coefficient is much reduced compared to free fluorescein. With 4 μM of fluorescein, a KD of 178 ± 93 μM BSA was obtained (mean ± SD).

5.4.3 Live Cells Application

Lastly, we employed the LIM technique to investigate MCF10A cells that were over-expressing Arc-EGFP, a protein known as Activity-regulated cytoskeleton-associated protein (Arc) or Arg 3.1 (Activity-regulated gene 3.1). Arc plays a crucial role in synaptic plasticity and is essential for the formation of long-term memory. It is found not only in the cytoplasm

but also accumulates in the nucleus, where it functions as a transcriptional regulator. In a recent study using raster image correlation spectroscopy (RICS), we discovered that nuclear Arc exhibited higher diffusivity compared to cytoplasmic Arc. However, RICS, similar to single point FCS, is limited to nanomolar concentrations unless combined with super-resolution techniques[96]. To validate the application of the LIM method to live cells, we imaged MCF10A cells expressing Arc-EGFP in various cellular locations. The cell nucleus was co-stained with NucBlue to enable differentiation between nuclear and cytoplasmic Arc-EGFP. An example LIM plot is depicted in Fig. 5.4 c, while Fig. 5.4 a and 5.4 b show the corresponding images. Our findings revealed an average diffusion coefficient of 3.0 $\mu m^2/s$ for the cytoplasm, whereas the nucleus exhibited significantly faster diffusion with an average of 8.8 $\mu m^2/s$ (Fig. 5.4 d). These results confirmed the trend we had previously observed using RICS[97]. Correlation methods not only provide insights into particle dynamics but can also estimate average concentrations based on the correlation function amplitude and the size of the observation volume. However, similar to RICS, the subtraction of the immobile fraction affects the correlation function amplitude, making accurate measurements of absolute concentrations challenging. Nevertheless, relative concentrations can still be determined, and our results indicated that the average Arc-EGFP concentration in the nucleus was approximately 6-fold higher than in the cell cytoplasm. It is worth noting that our LIM measurements were conducted

on cells cultured in a collagen matrix in a 3D environment, which differs from the conventional 2D cell plating used in the RICS experiments.

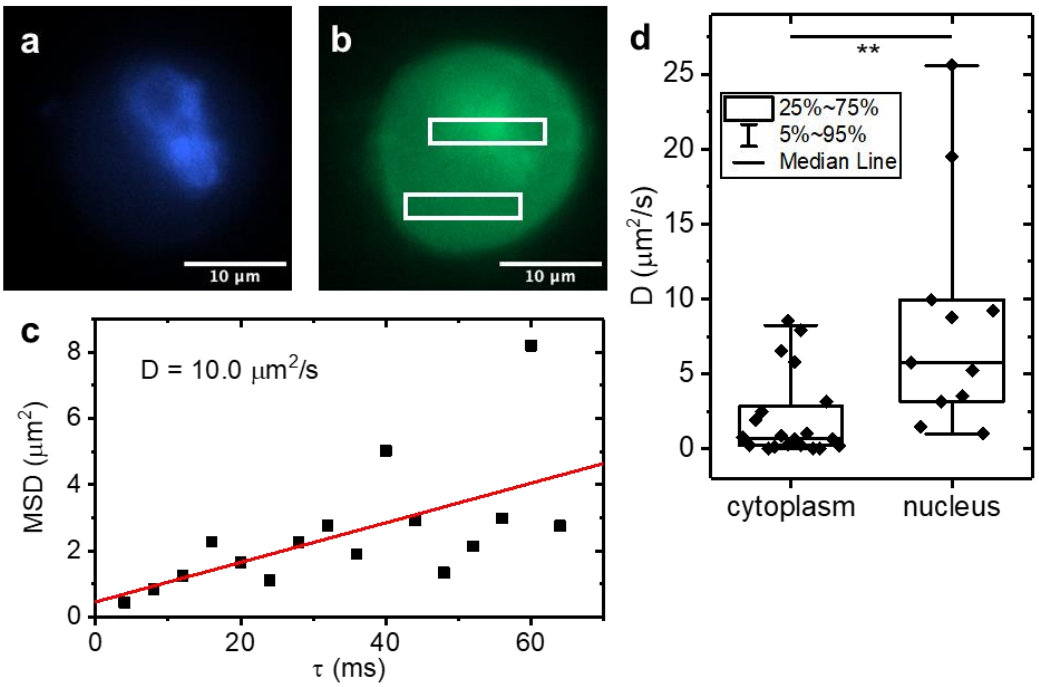

Figure 5. 4 Diffusion coefficients of Arc-EGFP measured in MCF10A cells. Line-MSD applied to 3D cultured MCF10A cells expressing Arc-EGFP. a) Example fluorescence image of NucBlue nuclear stain and b) Arc-EGFP of a single cell. c) Example LIM data of Arc-EGFP diffusion. d) Diffusion coefficients were measured in nucleus and in the cytoplasm. Box plots show the median ± interquartile ranges. Significantly faster Arc-EGFP diffusion was found in the nucleus compared to the cell cytoplasm ($p = 0.0075$, unpaired two sample t test, $N = 20$).

5.5 Discussion

The primary factor enabling Line-MSD to measure highly concentrated samples is the superior saturation capacity of a sCMOS sensor in comparison to a PMT. PMTs typically have maximum tolerable photon count rates of around 10 MHz. Consequently, when dealing with high fluorophore concentrations, the excitation light intensity must be reduced to prevent PMT saturation. However, this reduction in excitation intensity leads to a lower photon flux emitted

by each observed molecule. On the other hand, typical CMOS camera pixels have a well depth of 12 bits, with 11 bits available for analog-to-digital conversion (ADC), offering the ability to distinguish approximately 1000 values in a single readout cycle. Thus, when reading just a few lines of the sensor at a readout rate of approximately 10,000 Hz, a single camera pixel can match the PMT count rate of roughly 10 MHz. By simultaneously exposing and reading over 100 pixels in a single line, we can leverage much higher excitation intensities at high fluorophore concentrations without saturating the detector. Unlike a PMT detector, the appropriate utilization of a CMOS camera sensor enables the maintenance of a high photon yield per molecule even at high concentrations. This capability ultimately plays a critical role in determining the signal-to-noise ratio of the resulting correlation function.

CHAPTER 6: SUMMARY AND FUTURE DIRECTIONS

As like many biomedical engineers, my goal is to create tools to bridge the understanding of questions toward the deep biological field that remain unresolved. This dissertation described innovative methods to accomplish analyzing various aspects of mitochondria transfer and realize the importance of those aspects to other potential applications. To build those methods, one needs to start from scratch to get familiar with the background and needs to improve the current existing tools. Hence, the majority of this work was enhanced and optimized based on methods learned from the Laboratory for Fluorescence Dynamics.

In Chapter 2, I first shadowed literature review procedures to reveal mitochondria transfer in co-culture. However, this ended up to low transfer rate between cells and risk of staining dye diffusion across the imaging well. To avoid problems mentioned above, I turned into the use of transfection labeling and artificial mitochondria isolation approach. This enabled sufficient and stable freshly isolated mitochondria and tracking inside of host cells. By utilizing the recently existing tool, MitoMeter, developed by Dr. Austin Lefebvre, I was able to track and analyze mitochondrial dynamics to interpret behaviors of newly formed mitochondria which suggests increasing activity of mitophagy to selectively clear dysfunction mitochondria. Although knowing the dynamics of mitochondria give cue to possible cellular metabolic activities, it serves as an indirect finding instead of results from metabolic assays. Notably, XTT assays showed that although increasing proliferation rate of BCCs, mitochondria transfer

builds up ROS levels caused by boosted respiration rate which surpasses BCC tolerance of oxidative stress and collapses defense mechanism against anticancer drugs resulting in relatively more sensitive drug dosage response than controls. This finding stands critical in the perspective of using mitochondria transfer as potential therapeutic application against cancers. In Chapter 3, I started to apply the phasor approach to NADH FLIM and revealed the phasor shift from relatively free to bound fraction of NADH in single BCCs with additional mitochondria. This finding was supported by other well-known metabolic assays such as Seahorse and mitochondrial membrane potential analysis which further confirms the accuracy of lifetime imaging. However, the spatial information of FLIM was far more useful than pseudo coloring only single cells. I took advantage of the NADH autofluorescence signal to mask out single mitochondria in FLIM images by developing an image processing tool, FIBIS. It overcomes the disadvantage of frame scanning causing motion blur and saturation performing a 35% increase in image similarity referenced by fluorescent labeled images. Metabolic profiling of single mitochondria could be achieved and used to measure effects of metabolic inhibitors or in this dissertation, newly formed mitochondria. Another experiment by combining mitochondria transfer and OXPHOS inhibitors (Rotenone, Antimycin A, or FCCP) also showed the restriction of percentage change of bound NADH which clearly confirms the direction of metabolism after mitochondria transfer. In addition, FIBIS is under integration

with MitoMeter and can analyze morphology parameters such as length, branching, and numbers to acquire measurements all in one application.

In Chapter 4, the collaboration with Dr. Shiraiwa's group engages on ROS levels and their impact to macrophages. In our work, we demonstrated that gaining superoxide produced from NADPH oxidase causes damage to the cell membrane. To verify, we applied the use of THG imaging and revealed increasing lipid droplets surfacing from cell membrane and Laurdan lifetime analysis to indicate disorder of bilipid layer. Each approach suggests that the cell membrane was attacked by free radicals (superoxide) and transformed the cell to a more vulnerable condition to water in environment. The phasor approach to NAD(P)H FLIM results verify that NADPH oxidase locates at the cell membrane. By measuring the fraction of free and bound NAD(P)H in different time points, increase in free fraction NADPH follows a time dependent curve which is positively correlated with the superoxide production rate. This was, to the best of our knowledge, the first project to demonstrate phasor approach to FLIM measuring time sensitive dynamic changes of free and bound fraction NAD(P)H. Further investigation was done to reveal potential long lifetime species in the NAD(P)H emission spectrum as marker of oxidative stress. In short, the assay we developed provides an insight for recognition of lipid peroxidation which benefits the quantification of ROS damage.

Finally, in Chapter 5, we propose a customized microscopy system to improve the measurement of FCS, side-SPIM[29] and proved that camera-based detectors were capable of

higher pixel saturation to overcome the concentration limits of dyes when measuring fluctuation. The line-MSD method designed by Dr. Per Niklas Hedde, is based on observing a plane instead of volume from the point spread function in single point FCS which requires to be calibrated every time before measurements. The scanning plane requires only the time interval of camera exposure time and pixel size of the image to perform STICS calculation. One of the other advantages using side-SPIM is the degree of freedom it contains compared to regular SPIM setup systems. Magnetic sample holder enables the window chamber to move around the platform without risking to damage objectives or make contact with culture media and can switch between wells for different sample groups. Side-SPIM was able to measure diffusion coefficient of Atto 488 300 folds concentration higher than single point FCS measurements around 30μM. The convenience of line-MSD was demonstrated in biological applications such as binding efficiency, live cell transportation, and also applied to transferred mitochondria tracking in 3D which has been validated to image spheroids cultured in collagen type I. Further improvements such as the incubation system is necessitated for longer acquiring time. Another improvement needed is the channel switching system since camera detection system create channels by filter exchange which is based on Arduino controlled filter wheels. Optimization of scanning and exposure time is involved to meetup with 4D time-lapse image requirements.

Overall, this dissertation has covered the aspects of mitochondria transfer from biological assays, microscopy imaging, and software coding. The impact of mitochondria transfer includes both positive and negative results which encourages the candidate position for therapeutic application. While significant results were shown in 2D cell culture, 3D culture models have just barely begun to be investigated. To respond to that need, mitochondrial dynamics in 3D can be acquired by the side-SPIM system discussed in Chapter 5. By fine tuning Arduino switch controls of filters and excitation lasers in the MicroManager, we can achieve dual channel for host cell and transferred mitochondria targeting and sliced z plane timelapse images. Later, MitoMeter will be able to analyze data in 3D mode for comparison with 2D models. The side-SPIM system provides not only timelapse images but also our next generation of phasor approach to FLIM in 3D. To achieve the goal, we are installing FLIM cameras to synchronize with two photon excitation laser frequency reaching at 80MHz. Another goal to achieve is to smooth out background noise caused by DC charges of the camera where pixel information needs to be maintained as much as possible to perform FIBIS algorithm. All advancements mentioned above leads to a multi-function microscopy system which can robustly analyze cell or tissue samples of their FLIM or fluorescence related features towards either drug screening or metabolic inhibitor studies.

The application of mitochondria transfer is far from merely focusing on various types of breast cancer but many other mitochondrial dysfunction related diseases such as neurodegenerative

disorder[98,99] (Parkinson's, Alzheimer's, or Huntington's), heart conditions[100] (myocardial infarction), liver diseases[101] (non-alcoholic fatty liver disease), and metabolic disorders[102] (diabetes and obesity). My work has answered only a few questions existing in the biological field, but with the tools created, I hope my contribution will shed light towards the many bright scientists to develop even more innovative approaches based on FIBIS to understand live cell imaging and mitochondria transfer.

References

1. Rustom, A., Saffrich, R., Markovic, I., Walther, P. & Gerdes, H.-H. *Nanotubular Highways for Intercellular Organelle Transport*. http://science.sciencemag.org/.
2. Liu, D. *et al.* Intercellular mitochondrial transfer as a means of tissue revitalization. *Signal Transduction and Targeted Therapy 2021 6:1* **6**, 1–18 (2021).
3. Liu, Z., Sun, Y., Qi, Z., Cao, L. & Ding, S. Mitochondrial transfer/transplantation: an emerging therapeutic approach for multiple diseases. *Cell & Bioscience 2022 12:1* **12**, 1–29 (2022).
4. Caicedo, A., Aponte, P. M., Cabrera, F., Hidalgo, C. & Khoury, M. Artificial Mitochondria Transfer: Current Challenges, Advances, and Future Applications. *Stem Cells International* vol. 2017 Preprint at https://doi.org/10.1155/2017/7610414 (2017).
5. Yang, Y.-W. & Koob, M. D. Transferring isolated mitochondria into tissue culture cells. doi:10.1093/nar/gks639.
6. Sercel, A. J. *et al.* Stable transplantation of human mitochondrial DNA by high-throughput, pressurized isolated mitochondrial delivery. *Elife* **10**, 1–45 (2021).
7. Patananan, A. N. *et al.* Pressure-Driven Mitochondrial Transfer Pipeline Generates Mammalian Cells of Desired Genetic Combinations and Fates. *Cell Rep* **33**, 108562 (2020).
8. Wu, T. H. *et al.* Mitochondrial Transfer by Photothermal Nanoblade Restores Metabolite Profile in Mammalian Cells. *Cell Metab* **23**, 921–929 (2016).
9. Lin, H. C., Liu, S. Y., Lai, H. S. & Lai, I. R. Isolated mitochondria infusion mitigates ischemia-reperfusion injury of the liver in rats. *Shock* **39**, 304–310 (2013).
10. Spees, J. L., Olson, S. D., Whitney, M. J. & Prockop, D. J. *Mitochondrial transfer between cells can rescue aerobic respiration*. www.pnas.orgcgidoi10.1073pnas.0510511103 (2005).
11. Torralba, D., Baixauli, F. & Sánchez-Madrid, F. Mitochondria know no boundaries: Mechanisms and functions of intercellular mitochondrial transfer. *Frontiers in Cell and Developmental Biology* vol. 4 Preprint at https://doi.org/10.3389/fcell.2016.00107 (2016).
12. Caicedo, A., Aponte, P. M., Cabrera, F., Hidalgo, C. & Khoury, M. Artificial Mitochondria Transfer: Current Challenges, Advances, and Future Applications. *Stem Cells International* vol. 2017 Preprint at https://doi.org/10.1155/2017/7610414 (2017).
13. Zampieri, L. X., Silva-Almeida, C., Rondeau, J. D. & Sonveaux, P. Mitochondrial Transfer in Cancer: A Comprehensive Review. *Int J Mol Sci* **22**, (2021).
14. Caicedo, A. *et al.* MitoCeption as a new tool to assess the effects of mesenchymal stem/stromal cell mitochondria on cancer cell metabolism and function. *Sci Rep* **5**, (2015).

15. Kidwell, C. U. *et al.* Transferred mitochondria accumulate reactive oxygen species, promoting proliferation. *Elife* **12**, (2023).
16. Walker, M. A. & Tian, R. NAD(H) in mitochondrial energy transduction: implications for health and disease. *Curr Opin Physiol* **3**, 101–109 (2018).
17. Liou, G. Y. & Storz, P. Reactive oxygen species in cancer. *Free Radic Res* **44**, 479–496 (2010).
18. Tarafdar, A. & Pula, G. Molecular Sciences The Role of NADPH Oxidases and Oxidative Stress in Neurodegenerative Disorders. *J. Mol. Sci* **19**, 3824 (2018).
19. Chung, H. Y. *et al.* Xanthine dehydrogenase/xanthine oxidase and oxidative stress. *Age (Omaha)* **20**, 127 (1997).
20. Zorov, D. B., Juhaszova, M. & Sollott, S. J. Mitochondrial Reactive Oxygen Species (ROS) and ROS-Induced ROS Release. *Physiol Rev* **94**, 909–950 (2014).
21. Liu, Z. *et al.* Role of ROS and Nutritional Antioxidants in Human Diseases. *Front Physiol* **9**, (2018).
22. Santi, P. A. Light Sheet Fluorescence Microscopy: A Review. *Journal of Histochemistry and Cytochemistry* **59**, 129 (2011).
23. Trinh, A. L. *et al.* Tracking functional tumor cell subpopulations of malignant glioma by phasor fluorescence lifetime imaging microscopy of NADH. *Cancers (Basel)* **9**, (2017).
24. Ma, N. *et al.* Label-free assessment of pre-implantation embryo quality by the Fluorescence Lifetime Imaging Microscopy (FLIM)-phasor approach. *Sci Rep* **9**, (2019).
25. Stringari, C. *et al.* Metabolic trajectory of cellular differentiation in small intestine by Phasor Fluorescence Lifetime Microscopy of NADH. *Scientific Reports 2012 2:1* **2**, 1–9 (2012).
26. Stringari, C. *et al.* Phasor approach to fluorescence lifetime microscopy distinguishes different metabolic states of germ cells in a live tissue. *Proc Natl Acad Sci U S A* **108**, 13582–13587 (2011).
27. Ranjit, S., Malacrida, L., Stakic, M. & Gratton, E. Determination of the metabolic index using the fluorescence lifetime of free and bound nicotinamide adenine dinucleotide using the phasor approach. *J Biophotonics* **12**, (2019).
28. Huang, Y. *et al.* Phasor approach FLIM as an indicator for NADPH oxidase during exposure to secondary organic aerosols. *Biophysj* **121**, 415a (2022).
29. Huang, Y.-K. ;, Hedde, P. N., Mironov, A., Huang, Y.-K. & Niklas Hedde, P. Breaking the Concentration Limit in Fluorescence Fluctuation Spectroscopy with Camera-Based Detection. *International Journal of Molecular Sciences 2022, Vol. 23, Page 9840* **23**, 9840 (2022).

30. Chang, J. C. *et al.* Mitochondrial transplantation regulates antitumour activity, chemoresistance and mitochondrial dynamics in breast cancer. *Journal of Experimental and Clinical Cancer Research* **38**, (2019).
31. Federico, A. *et al.* Mitochondria, oxidative stress and neurodegeneration. *J Neurol Sci* **322**, 254–262 (2012).
32. Jeong, S. Y. & Seol, D. W. The role of mitochondria in apoptosis. *BMB Rep* **41**, 11–22 (2008).
33. Hekmatshoar, Y., Nakhle, J., Galloni, M. & Vignais, M. L. The role of metabolism and tunneling nanotube-mediated intercellular mitochondria exchange in cancer drug resistance. *Biochemical Journal* vol. 475 2305–2328 Preprint at https://doi.org/10.1042/BCJ20170712 (2018).
34. Wang, X. & Gerdes, H. H. Transfer of mitochondria via tunneling nanotubes rescues apoptotic PC12 cells. *Cell Death Differ* **22**, 1181–1191 (2015).
35. Pour, P. A., Kenney, M. C. & Kheradvar, A. Bioenergetics consequences of mitochondrial transplantation in cardiomyocytes. *J Am Heart Assoc* **9**, (2020).
36. Kim, M. J., Hwang, J. W., Yun, C. K., Lee, Y. & Choi, Y. S. Delivery of exogenous mitochondria via centrifugation enhances cellular metabolic function. *Sci Rep* **8**, (2018).
37. Newell, C. *et al.* Mesenchymal stem cells shift mitochondrial dynamics and enhance oxidative phosphorylation in recipient cells. *Front Physiol* **9**, (2018).
38. Li, C. J., Chen, P. K., Sun, L. Y. & Pang, C. Y. Enhancement of Mitochondrial Transfer by Antioxidants in Human Mesenchymal Stem Cells. *Oxid Med Cell Longev* **2017**, (2017).
39. Gäbelein, C. G. *et al.* Mitochondria transplantation between living cells. *bioRxiv* 2021.11.09.467932 (2021) doi:10.1101/2021.11.09.467932.
40. Spink, B. C. *et al.* Inhibition of MCF-7 breast cancer cell proliferation by MCF-10A breast epithelial cells in coculture. *Cell Biol Int* **30**, 227–238 (2006).
41. Ivers, L. P. *et al. Dynamic and influential interaction of cancer cells with normal epithelial cells in 3D culture*. *Cancer Cell International* vol. 14 http://www.cancerci.com/content/14/1/108 (2014).
42. Elliott, R. L., Jiang, X. P. & Head, J. F. Mitochondria organelle transplantation: Introduction of normal epithelial mitochondria into human cancer cells inhibits proliferation and increases drug sensitivity. *Breast Cancer Research and Treatment* vol. 136 347–354 Preprint at https://doi.org/10.1007/s10549-012-2283-2 (2012).
43. Dimri, G., Band, H. & Band, V. Mammary epithelial cell transformation: Insights from cell culture and mouse models. *Breast Cancer Research* **7**, 171–179 (2005).

44. Ivers, L. P. *et al. Dynamic and influential interaction of cancer cells with normal epithelial cells in 3D culture*. *Cancer Cell International* vol. 14 http://www.cancerci.com/content/14/1/108 (2014).
45. Cell Metabolism | Learn Science at Scitable. https://www.nature.com/scitable/topicpage/cell-metabolism-14026182/.
46. Warburg, O. On the origin of cancer cells. *Science (1979)* **123**, 309–314 (1956).
47. Caines, J. K., Barnes, D. A. & Berry, M. D. The Use of Seahorse XF Assays to Interrogate Real-Time Energy Metabolism in Cancer Cell Lines. doi:10.1007/978-1-0716-2376-3_17.
48. Rovini, A. *et al.* Quantitative analysis of mitochondrial membrane potential heterogeneity in unsynchronized and synchronized cancer cells. *The FASEB Journal* **35**, e21148 (2021).
49. Digman, M. A., Caiolfa, V. R., Zamai, M. & Gratton, E. The Phasor Approach to Fluorescence Lifetime Imaging Analysis. *Biophys J* **94**, L14–L16 (2008).
50. Jabłoństski, A. Efficiency of Anti-Stokes Fluorescence in Dyes. *Nature 1933 131:3319* **131**, 839–840 (1933).
51. Weber, G. Resolution of the fluorescence lifetimes in a heterogeneous system by phase and modulation measurements. *Journal of Physical Chemistry* **85**, 949–953 (1981).
52. Jameson, D. M., Gratton, E. & Hall, R. D. The Measurement and Analysis of Heterogeneous Emissions by Multifrequency Phase and Modulation Fluorometry The Measurement and Analysis of Heterogeneous Emissions by Multifrequency Phase and Modulation Fluorometr. *Appl Spectrosc Rev* **20**, 55–106 (1984).
53. Ma, N., Digman, M. A., Malacrida, L. & Gratton, E. Measurements of absolute concentrations of NADH in cells using the phasor FLIM method. *Biomed Opt Express* **7**, 2441 (2016).
54. Lakowicz, J. R., Szmacinski, H., Nowaczyk, K. & Johnson, M. L. *Fluorescence lifetime imaging of free and protein-bound NADH*. *Biochemistry* vol. 89 https://www.pnas.org (1992).
55. Ranjit, S., Datta, R., Dvornikov, A. & Gratton, E. Multicomponent Analysis of Phasor Plot in a Single Pixel to Calculate Changes of Metabolic Trajectory in Biological Systems. *J Phys Chem A* **123**, 9865–9873 (2019).
56. Perry, S. W., Norman, J. P., Barbieri, J., Brown, E. B. & Gelbard, H. A. Mitochondrial membrane potential probes and the proton gradient: A practical usage guide. *Biotechniques* **50**, 98–115 (2011).
57. Lelieveld, S. *et al.* Hydroxyl Radical Production by Air Pollutants in Epithelial Lining Fluid Governed by Interconversion and Scavenging of Reactive Oxygen Species. *Cite This: Environ. Sci. Technol* **55**, 14069–14079 (2021).

58. Hayyan, M., Ali Hashim, M. & AlNashef, I. M. Superoxide Ion: Generation and Chemical Implications. (2016) doi:10.1021/acs.chemrev.5b00407.
59. Babior, B. M. Superoxide: a two-edged sword. *Brazilian Journal of Medical and Biological Research* **30**, 141–155 (1997).
60. Auten, R. L. & Davis, J. M. Oxygen Toxicity and Reactive Oxygen Species: The Devil Is in the Details. *Pediatric Research 2009 66:2* **66**, 121–127 (2009).
61. Snezhkina, A. V. *et al.* ROS Generation and Antioxidant Defense Systems in Normal and Malignant Cells. *Oxid Med Cell Longev* **2019**, (2019).
62. Matés, J. M. Effects of antioxidant enzymes in the molecular control of reactive oxygen species toxicology. *Toxicology* **153**, 83–104 (2000).
63. Jimenez, J. L. *et al.* Evolution of organic aerosols in the atmosphere. *Science (1979)* **326**, 1525–1529 (2009).
64. Wennberg, P. O. *et al.* Gas-Phase Reactions of Isoprene and Its Major Oxidation Products. (2018) doi:10.1021/acs.chemrev.7b00439.
65. Claeys, M. *et al.* Formation of Secondary Organic Aerosols Through Photooxidation of Isoprene. *Science (1979)* **303**, 1173–1176 (2004).
66. Lakey, P. S. J. *et al.* Chemical exposure-response relationship between air pollutants and reactive oxygen species in the human respiratory tract OPEN. *Nature Publishing Group* (2016) doi:10.1038/srep32916.
67. Fang, T., Lakey, P. S. J., Weber, R. J. & Shiraiwa, M. Oxidative Potential of Particulate Matter and Generation of Reactive Oxygen Species in Epithelial Lining Fluid. *Environ Sci Technol* **53**, 12784–12792 (2019).
68. Forman, H. J. & Torres, M. Reactive oxygen species and cell signaling: respiratory burst in macrophage signaling. *Am J Respir Crit Care Med* **166**, (2002).
69. Beck-Speier, I. *et al.* Oxidative stress and lipid mediators induced in alveolar macrophages by ultrafine particles. *Free Radic Biol Med* **38**, 1080–1092 (2005).
70. Gurgueira, S. A., Lawrence, J., Coull, B., Krishna Murthy, G. G. & González-Flecha, B. Rapid increases in the steady-state concentration of reactive oxygen species in the lungs and heart after particulate air pollution inhalation. *Environ Health Perspect* **110**, 749–755 (2002).
71. Panday, A., Sahoo, M. K., Osorio, D. & Batra, S. NADPH oxidases: an overview from structure to innate immunity-associated pathologies. (2015) doi:10.1038/cmi.2014.89.
72. Kuwabara, W. M. T. *et al.* NADPH Oxidase-Dependent Production of Reactive Oxygen Species Induces Endoplasmatic Reticulum Stress in Neutrophil-Like HL60 Cells. *PLoS One* **10**, (2015).
73. Blacker, T. S. & Duchen, M. R. Investigating mitochondrial redox state using NADH and NADPH autofluorescence. *Free Radic Biol Med* **100**, 53–65 (2016).

74. Togashi, D. M. & Nicodem, D. E. Photophysical studies of 9,10-phenanthrenequinones. *Spectrochim Acta A Mol Biomol Spectrosc* **60**, 3205–3212 (2004).
75. Scheinpflug, K., Krylova, O. & Strahl, H. Measurement of cell membrane fluidity by Laurdan GP: Fluorescence spectroscopy and microscopy. *Methods in Molecular Biology* **1520**, 159–174 (2017).
76. Golfetto, O., Hinde, E. & Gratton, E. Laurdan Fluorescence Lifetime Discriminates Cholesterol Content from Changes in Fluidity in Living Cell Membranes. *Biophys J* **104**, 1238 (2013).
77. Dvornikov, A., Malacrida, L. & Gratton, E. The DIVER Microscope for Imaging in Scattering Media. *Methods Protoc* **2**, 1–12 (2019).
78. Datta, R., Alfonso-Garciá, A., Cinco, R. & Gratton, E. Fluorescence lifetime imaging of endogenous biomarker of oxidative stress. *Scientific Reports 2015 5:1* **5**, 1–10 (2015).
79. Togashi, D. M. & Nicodem, D. E. Photophysical studies of 9,10-phenanthrenequinones. *Spectrochim Acta A Mol Biomol Spectrosc* **60**, 3205–3212 (2004).
80. Magde, D., Elson, E. L. & Webb, W. W. Fluorescence correlation spectroscopy. II. An experimental realization. *Biopolymers* **13**, 29–61 (1974).
81. Jameson, D. M., Ross, J. A. & Albanesi, J. P. Fluorescence fluctuation spectroscopy: ushering in a new age of enlightenment for cellular dynamics. *Biophys Rev* **1**, 105–118 (2009).
82. Ruan, L. *et al.* A sensitive and microscale method for drug screening combining affinity probes and single molecule fluorescence correlation spectroscopy †. *Cite this: Analyst* **140**, 1207 (2015).
83. Eggeling, C. *et al.* Direct observation of the nanoscale dynamics of membrane lipids in a living cell. *Nature 2008 457:7233* **457**, 1159–1162 (2008).
84. Wenger, J. *et al.* Single molecule fluorescence in rectangular nano-apertures. *Opt Express* **13**, 7035 (2005).
85. Leutenegger, M. *et al.* Confining the sampling volume for Fluorescence Correlation Spectroscopy using a sub-wavelength sized aperture. *Optics Express, Vol. 14, Issue 2, pp. 956-969* **14**, 956–969 (2006).
86. Leutenegger, M. *et al.* The Photon Counting Histogram in Fluorescence Fluctuation Spectroscopy with Non-Ideal Photodetectors. *Eur. Biophys. J. Biophys. Lett* **22**, 18 (1993).
87. Koppel, D. E. Statistical accuracy in f1uorescence correlation spectroscopy*. *Phys Rev A (Coll Park)* **10**, (1974).

88. Laurence, T. A., Ly, S., Bourguet, F., Fischer, N. O. & Coleman, M. A. Fluorescence Correlation Spectroscopy at Micromolar Concentrations without Optical Nanoconfinement. (2014) doi:10.1021/jp505881z.
89. Hedde, P. N., Malacrida, L., Ahrar, S., Siryaporn, A. & Gratton, E. sideSPIM – selective plane illumination based on a conventional inverted microscope. *Biomed Opt Express* **8**, 3918 (2017).
90. Gendron, P.-O., Avaltroni, F. & Wilkinson, K. J. Diffusion Coefficients of Several Rhodamine Derivatives as Determined by Pulsed Field Gradient-Nuclear Magnetic Resonance and Fluorescence Correlation Spectroscopy. doi:10.1007/s10895-008-0357-7.
91. Hedde, P. N., Stakic, M. & Gratton, E. Rapid Measurement of Molecular Transport and Interaction inside Living Cells Using Single Plane Illumination. *Scientific Reports 2014 4:1* **4**, 1–6 (2014).
92. Di Rienzo, C., Gratton, E., Beltram, F. & Cardarelli, F. Fast spatiotemporal correlation spectroscopy to determine protein lateral diffusion laws in live cell membranes. *Proc Natl Acad Sci U S A* **110**, 12307–12312 (2013).
93. Mao, Y., Yu, L., Yang, R., Qu, L. B. & Harrington, P. D. B. A novel method for the study of molecular interaction by using microscale thermophoresis. *Talanta* **132**, 894–901 (2015).
94. Majorek, K. A. *et al.* Structural and immunologic characterization of bovine, horse, and rabbit serum albumins. *Mol Immunol* **52**, 174–182 (2012).
95. Levi, V. & González Flecha, F. L. Reversible fast-dimerization of bovine serum albumin detected by fluorescence resonance energy transfer. *Biochim Biophys Acta* **1599**, 141–148 (2002).
96. Hedde, N. *et al.* ARTICLE Stimulated emission depletion-based raster image correlation spectroscopy reveals biomolecular dynamics in live cells. *Nat Commun* (2013) doi:10.1038/ncomms3093.
97. Hedde, P. N., Barylko, B., Binns, D. D., Jameson, D. M. & Albanesi, J. P. Differential Mobility and Self-Association of Arc/Arg3.1 in the Cytoplasm and Nucleus of Living Cells. *ACS Chem Neurosci* **13**, 876–882 (2022).
98. Nitzan, K. *et al.* Mitochondrial Transfer Ameliorates Cognitive Deficits, Neuronal Loss, and Gliosis in Alzheimer's Disease Mice. *J Alzheimers Dis* **72**, 587–604 (2019).
99. Flannery, P. J. & Trushina, E. Mitochondrial Dynamics and Transport in Alzheimer's Disease. *Mol Cell Neurosci* **98**, 109 (2019).
100. Sun, M. *et al.* Mitochondrial transplantation as a novel therapeutic strategy for cardiovascular diseases. *J Transl Med* **21**, 1–14 (2023).

101. Chen, Y. *et al.* Mitochondrial transplantation: opportunities and challenges in the treatment of obesity, diabetes, and nonalcoholic fatty liver disease. *Journal of Translational Medicine 2022 20:1* **20**, 1–16 (2022).
102. Louwagie, E. J., Larsen, T. D., Wachal, A. L., Gandy, T. C. T. & Baack, M. L. Mitochondrial Transfer Improves Cardiomyocyte Bioenergetics and Viability in Male Rats Exposed to Pregestational Diabetes. *International Journal of Molecular Sciences 2021, Vol. 22, Page 2382* **22**, 2382 (2021).